

BACHELOR PROJECT

K2: A SEARCH FOR EXOPLANETS AND VARIABLE STARS

BY

NICHOLAS E. JANNSEN



SUPERVISORS

FRANK GRUNDAHL
KARSTEN BROGAARD

DEPARTMENT OF PHYSICS AND ASTRONOMY
AARHUS UNIVERSITY
15. JUNE, 2015

Contents

Abstract	iii
Preface	iv
Introduction	v
1 Data and Missions	1
1.1 The Kepler Mission	1
1.2 K2 Data	1
2 Theory	3
2.1 Variable Stars	3
2.1.1 Fourier Spectra and Time Series Analysis	3
2.2 Exoplanet Transit Science	5
2.2.1 Geometry	6
2.2.2 Transit Times	7
2.2.3 Absolute Dimensions	7
2.2.4 Limb Darkening	8
3 Data Reduction	9
3.1 Data Exclusion	9
3.2 Aperture Photometry	10
3.3 Automated Preparation Pipeline	13
4 Results and Analysis	16
4.1 Photometric Precision	16
4.2 Main-Belt Asteroids	17
4.3 Variable Findings	19
4.4 Stellar Science of Host Star	21
4.4.1 Host Star Membership	21
4.4.2 Determination of Stellar Parameters	24
4.5 Exoplanet Candidate	25
4.5.1 Model-fit Light Curve	25
4.5.2 False Positives	27
4.5.3 Planetary Parameters	28
5 Discussion and Concluding Remarks	31
5.1 Ways to Improve the Photometric Precision	31
5.2 Aspects of the Future	32
5.3 Concluding Remarks	32

CONTENTS

Bibliography	33
A Appendix: Mission Information	36
B Appendix: Project Information	38
C Appendix: Results	41
C.1 Table of Findings	41
C.2 Light Curves	43

Abstract

English

The space telescope Kepler has with its extremely high photometric precision revolutionized the studies of exoplanets. With the initiation in 2014 of the new mode of observation called the K2 mission, the photometric quality did however decrease due to the spacecraft's inability to point precisely. However, the K2 mission provides an opportunity to continue Kepler's groundbreaking discoveries in the field of planetary science. Furthermore, it became the foundation for many new and exiting astrophysical studies.

In this project, I have explored the astrophysical diversity in data from the K2 mission. I have developed a program that effectively extracts photometric light curves for the targets of interest. For a further photometric improvement, a filter designed for the Kepler missions was added. The functionality of the combined routine was evident from our independent discovery of an exoplanet candidate as well as several variable stars. A detailed analysis of the planet candidate suggests a hot Jupiter-sized planet due to its radius and semimajor axis of $R_p = 1.08R_{\text{Jup}}$ and $a = 0.04 \text{ AU}$, respectively. However, future studies are needed in order to confirm the planet interpretation.

Dansk

Rumteleskopet Kepler har med sin ekstremt høje fotometriske præcision revolutioneret studierne af exoplaneter. Med den efterfølgende Kepler-mission i 2014, den såkaldte K2-mission, blev den fotometriske kvalitet forringet pga. rumfartøjets manglende evne til at pege præcist. På trods af dette gør K2-missionen det muligt at fortsætte Keplers banebrydende opdagelser indenfor planetfysik. Ligeledes danner det nu grundlag for mange nye og spændende astrofysiske studier generelt.

Jeg har i dette projekt udforsket den astrofysiske mangfoldighed, som K2-missionens data indeholder. Jeg har udviklet et program, der effektivt udtrækker fotometriske lyskurver for udvalgte objekter. Endvidere var et filter, designet til Kepler-missionerne, tilføjet for at opnå en forbedring af fotometriken. Funktionaliteten af det kombinerede program kunne tydeligt ses i min uafhængige opdagelse af en exoplanetkandidat samt flere variable stjerner. Ud fra det analyserede data af planetkandidaten lader det til at være en varm Jupiter-lignende planet pga. dens radius samt halve storakse af $R_p = 1.08R_{\text{Jup}}$ and $a = 0.04 \text{ AU}$, respektivt. Dog er fremtidige studier nødvendige for at bekræfte objektets status som planet.

Preface

This is my Bachelor project – the final outcome of my work with data collected by the space telescope Kepler, after the spacecraft entered a new mode of observation known as the K2 mission. The wealth of astrophysical phenomena hidden in this data have been a motivating guideline. This project demonstrates the continuous contributions of Kepler, here consisting of asteroids, exoplanets and variable stars.

To fully understand this project, a basic knowledge of astrophysics corresponding to the knowledge gained by the astronomical subject of study for the bachelor degree of physics at Aarhus University is assumed. Furthermore, a basic knowledge of vector-oriented programming is also assumed. Because I was favored by fortune to use an automated preparation pipeline developed in the program language Python, I developed some basic skills for this object-oriented language. These skills will surely be useful in future astrophysical projects, owing to the fact that this language is one of the most used – if not the most used language – by astronomers worldwide. This project has been typeset in \LaTeX where the layout has been inspired by Daleifs book¹ and the many \LaTeX communities online. I give my gratitude for their hard work – it is a dark art. Moreover, a thank goes to the KASOC community for the establishment of an understandable webpage where the K2 data can be downloaded freely.

I would like to use this opportunity to direct a great thank to Frank Grundahl and Karsten Brogaard for their patience and always useful advice and helpful input. From my point of view it has been a wonderful collaboration. As well I would like to thank Nardiello and his group for getting the chance to use their results from their multi-year survey aimed at collecting high-precision photometry at the same field of interest. Though my observational experience is more limited, I still recognize the hard work, the long nights and the troublesomeness in making ground based observation. A great thank goes to Rasmus Handberg and Mikkel Lund for their generosity of handing me a fused version of their automated preparation pipeline designed for the Kepler data and the pipeline K2P² designed for K2 data. Moreover, a thank goes to Ditte Slumstrup for using the FIES spectrograph on NOT to measure a desired spectra. Lastly, a thank goes to my girlfriend Amalie for her everyday support and linguistic guidance.

Nicholas Emborg Jannsen
nicholasemborgjannsen@hotmail.com
Aarhus, June 15th, 2015

¹<http://data.math.au.dk/system/latex/bog/version3/beta/ltxb-2011-09-13-20-10.pdf>

Introduction

When we astronomers explore the universe, we are dazzled by the billions and billions sources of light that illuminate the cosmic arena. Launching a telescope out into space for the examination of these light sources is favoured due to a non-existing atmospheric disturbance² in space, but unfavored by the great expense space missions have. Besides the high photometric precision, space telescopes can operate undisturbed by the day-and-night cycle and yearly apparent movement of objects as Earth based observations suffer from³.

An example of a space mission that have revolutionized our view of astrophysical science is the Kepler mission. As its primary goal to determine the frequency of Earth-like planets around Sun-like stars, Kepler has, since its first observations, expanded the science of extra solar planets; exoplanets. The first exoplanets ever discovered were Jupiter-mass objects in short-period orbits due to their large radial velocity signal. However, in 2012 the first Earth-like planet in the habitable zone, Kepler-22b, was discovered [4]. Because of Kepler and related space missions, 1888 exoplanets have been discovered out of which 1187 are in single planetary systems and 477 are in multiple planet systems⁴. Another application is that Kepler observations can be used for asteroseismic analysis. Today asteroseismology – the science of stellar oscillations – is the most profound technique to compute fundamental stellar parameters and test stellar structure and evolution models, as the modes of oscillation serves to probe the interior of a star.

Signals that prevent exoplanet and asteroseismic science are routinely picked up by Kepler. Many might relate such signals to “noise”, however, signals belonging to stellar variability are hidden among. Historically the science of variable stars have had a major impact on understanding our place among the stars. E.g. stellar pulsating variables such as Cepheids and RR Lyraes have been used to provide precise measurements of cosmic distances. Moreover, eclipsing binaries have been a milestone in stellar astrophysics and have as well enabled computation of stellar parameters, test stellar evolution models and have also been used to determine cosmic distances [4]. When using the tools of Fourier analysis to analyze variable stars, multi-year coherent observations, which space telescopes such as Kepler can deliver, serves as a much better probe for any signal of variability.

This project deals with data from the space telescope Kepler after a secondary reaction wheel failed in May 2013 and preventing the continuation of the mission. In August 2013, Kepler entered a new observation mode called the K2 mission. With only two functional reaction wheels the K2 mission suffers from the spacecraft’s inability to point

²Such as the seeing condition (which depends on cloud cover, wind speed, humidity and dust level) and airmass.

³Due to Earths rotational period and orbital period around the Sun.

⁴<http://exoplanet.eu/>

INTRODUCTION

continuously and stable to a fixed field of view. Because the K2 data contains great challenges, this project has from the beginning been a “go-and-explore” project. However, we first attempted to focus on oscillations for red giant stars, but with an independent discovery of an exoplanet candidate and several new variable stars, we changed the goal for this project. Our discovery of the exoplanet candidate was unfortunately made one month later than the first discovery made by LaCourse et al. [16].

In this project we will first of all use variable stars from Nardiello et al.’s catalog [22] and our own variable findings to test the functionality of our routine developed for the K2 data and secondly try to confirm the planetary interpretation and estimate related parameters of the exoplanet candidate.

Chapter 1 gives a brief overview of the observational data associated with the K2 mission. In Chapter 2 a representation of the theoretical foundation is given. Chapter 3 will describe the development of the data reduction routine, followed by an analysis of our variety of results in Chapter 4. Lastly, Chapter 5 contains a discussion of the results plus proposed improvements and future projects. Chapter 5 will finish with concluding remarks.

“Second star to the right, and straight on till morning.”

– Peter Pan, 1904

1

Data and Missions

The Kepler Mission

On March 2009 the space telescope Kepler was launched to make observations of $\sim 170,000$ stars in a Field Of View (FOV) located between the constellation of Cygnus and Lyra ([4]; [2]). Its main task was to determine the frequency of Earth-like planets in or near the habitable zone around Sun-like stars as well as expand the studies of Eclipsing Binaries (EB) [15]. To fulfill this quest the spacecraft looked along the Orion Spur spiral arm of the Milky Way galaxy. The telescope is powered by solar cells and because of its heliocentric, Earth-trailing orbit the demands of observations of a fixed FOV for 4 or more years is ideal [15]. The overall scientific impact of Kepler is its ability to make very precise photometry for its long cadence and very large FOV. After an operation time of 4 years the telescope was unable to sustain a sufficient pointing stability to the original field due to a second broken reaction wheel. Luckily scientists found a new meta-stable configuration, where it now points along the ecliptic plane. This change in schedule is called the K2 mission and it have open the doors for new astrophysical studies with Kepler.

K2 Data

In this project the analyzed data was taken with the Kepler space telescope in connection to the K2 program. The data contains images of the open stellar clusters M35 (or NGC 2168) and NGC 2158, located in the constellation of the Twins, from the 3 months cadence of Spring 2014 – the so-called Champaign 0 (C0). As mentioned, the K2 mission suffers from pointing instability, as only two reaction wheels are operational. Due to the pressure of the solar wind, Kepler drifts over a period of approximately 6 hours, which reduces the photometric precession. However, because the drift motion is only along the spacecraft’s roll axis, stellar objects only moves in an arc upon Kepler’s CCDs, thus, making the effect easier to take into account. An appreciable pointing precession has shown not to hinder a precise photometry (see e.g [34]) and, accordingly, the K2 mission has been estimated to be capable of a precision of 80 parts per million (ppm), close to the sensitivity of the primary mission [1].

Kepler targets can be observed in a Long Cadence (LC) and a Short Cadence (SC) with an integration time of $\Delta t \sim 29.4$ min and $\Delta t \sim 58.89$ s, respectively. Only LC data will be analyzed in this project, whereas the SC data is especially interesting for asteroseismic

1.2 K2 DATA

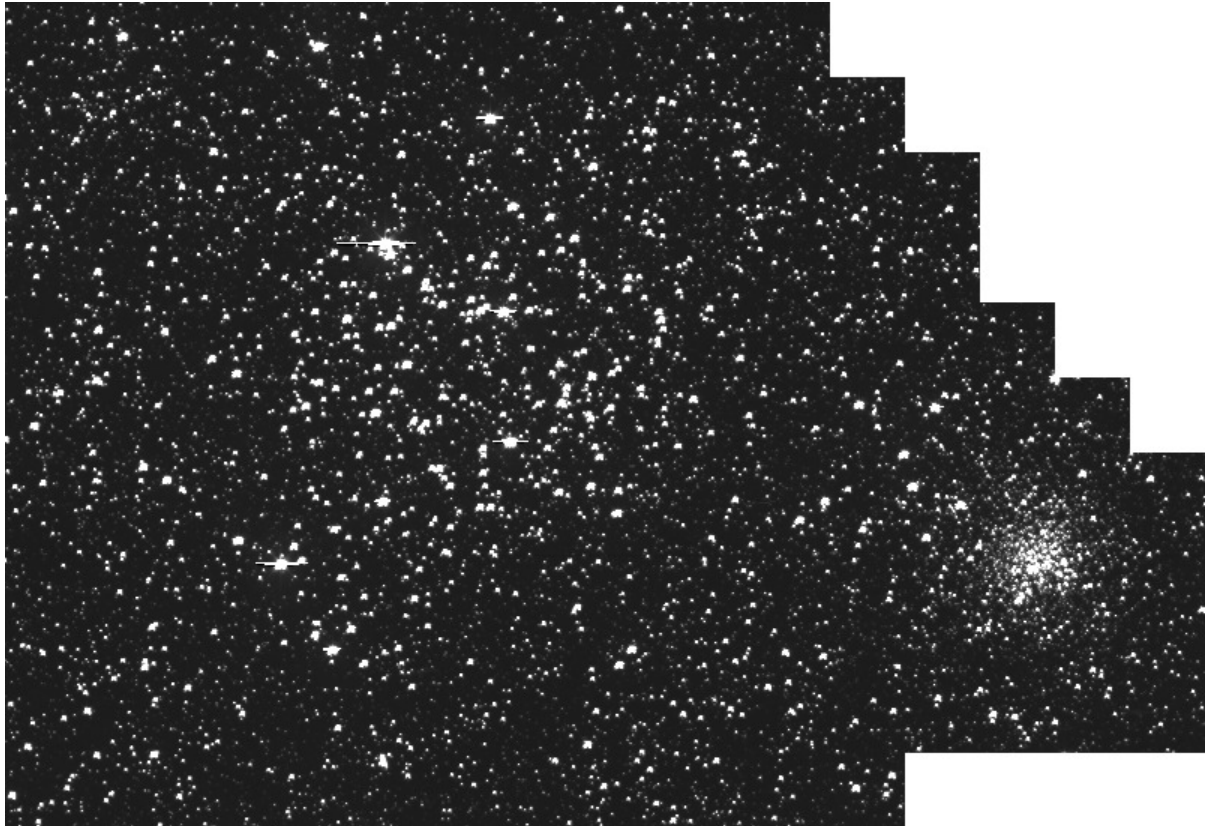


Figure 1.1: This figure shows an image, constructed in this project, of the two globular clusters M35 and NGC 2158 combined by 154 separate 50×50 pixel masks. Each pixel mask has a dimension of about $3.3' \times 3.3'$ and the combined image has a FOV of about $36.5' \times 53.1'$ in its widest dimensions.

research [12]. All data is from the Kepler Asteroseismic Science Operations Center (KASOC) database¹ in connection to the yearly Guest Observer (GO) program. The aperture diameter of 0.95 meter is designed so that it can collaborate with the 95 mega pixel detectors to encompass its $\sim 12^\circ \times 12^\circ$ FOV. The CCDs are read out in half a second without a shutter. Because every pixel in a CCD column passes under every piece of sky in a column during a read out, this results in smearing effects. As seen in figure 1.1, the available data is an image combined of 154 separate $50 \times 50 \times 3753$ Target Pixel Frames (TPF) over the most dense region of M35 and NGC 2158. This figure is a product of this project². Unlike most conventional telescopes, Kepler has large pixels and thus a rather broad Point Spread Function (PSF)³ of about 6 pixels. The big *plate scale* of $3.98''$ per pixel is due to the requirement of a large FOV and technical requirements such as low electronic shot noise⁴ and minimization of photometric sensitivity [15]. Depending on the pixel-to-pixel sensitivity over the CCDs, stars brighter than a magnitude of 12 will saturate with an exposure time of only 5 seconds [15]. This means that some stars in the LC data undeniably will be saturated, which is in agreement with the 5 easily identified bleed-out stars in figure 1.1. All stated informations in this Chapter can be found in Appendix A.

¹<http://kasoc.au.dk/>

²Because no stamp ordering was made before hand, it has literary been a puzzle to piece this image together, however, coordinates of variable stars in the same FOV (from [22]) helped to pinpoint each TPF.

³The PSF describes the response of an imaging system to a point source [6]

⁴Also called Poisson noise which is present in optical devices due to the associated particle nature of light [6].

*"I will love the light for it shows
me the way; yet I will love the
darkness for it shows me the stars."*

– Augustine Og Mandino, 1972

2

Theory

Variable Stars

This section is mainly based on the knowledge I have obtained through the master course *Variable Stars: from classical pulsations to eclipsing binaries*. Only lecture slides were used and if these are needed, please contact lecturer Victoria Antoci. This section is not intended to give a detailed description of the physical mechanisms behind variable stars, rather it will serve as the foundation of the analysis of light curves later in the project.

Stars, which brightness change is not due to stellar evolution, and vary periodically, semi-periodically or irregularly on time scales of less than seconds to centuries, are defined as variable stars. The physical mechanism behind the signal of variability determines the classification of these stars. Thus, besides testing stellar structure and evolution models, variable stars can also be used to probe different physical processes such as convection, nuclear synthesis, magnetic activity etc.. The method used to analyze any astrophysical signal of variability is called a *time series analysis*. When analyzing time series of periodic variable stars the most often used tool is a Fourier spectrum. In the following we will briefly discuss the *power* of this technique.

Fourier Spectra and Time Series Analysis

In some cases, when analyzing stellar time series the signal of variability cannot readily be determined from the light curve alone, and a Fourier spectrum is needed. Fourier analysis uses an infinite number of sine and cosine functions all with a different period, P , amplitude, A , and phase, Φ , to analyze a given set of time-varying data. Denoting the time series as $x(t)$ the Fourier transform is given by

$$F(\nu) = \int_{-\infty}^{\infty} x(t) e^{-2\pi i \nu t} dt, \quad (2.1)$$

where $i = \sqrt{-1}$ is the imaginary number, $\nu = 1/P$ is the frequency and t is the time. The importance of $F(\nu)$ is that if a time-coherent signal with a frequency of ν' is present in a time series, the Fourier transform will reach a local maximum (identified as a peak) in the Fourier spectrum at ν' . In the case of multiple signals with different frequencies a global maximum in the Fourier spectrum will be reached by the frequency signal showing the strongest correlation in the light curve [32]. Thus, from the Fourier transform the period of a periodic signal can easily be determined.

2.1 VARIABLE STARS

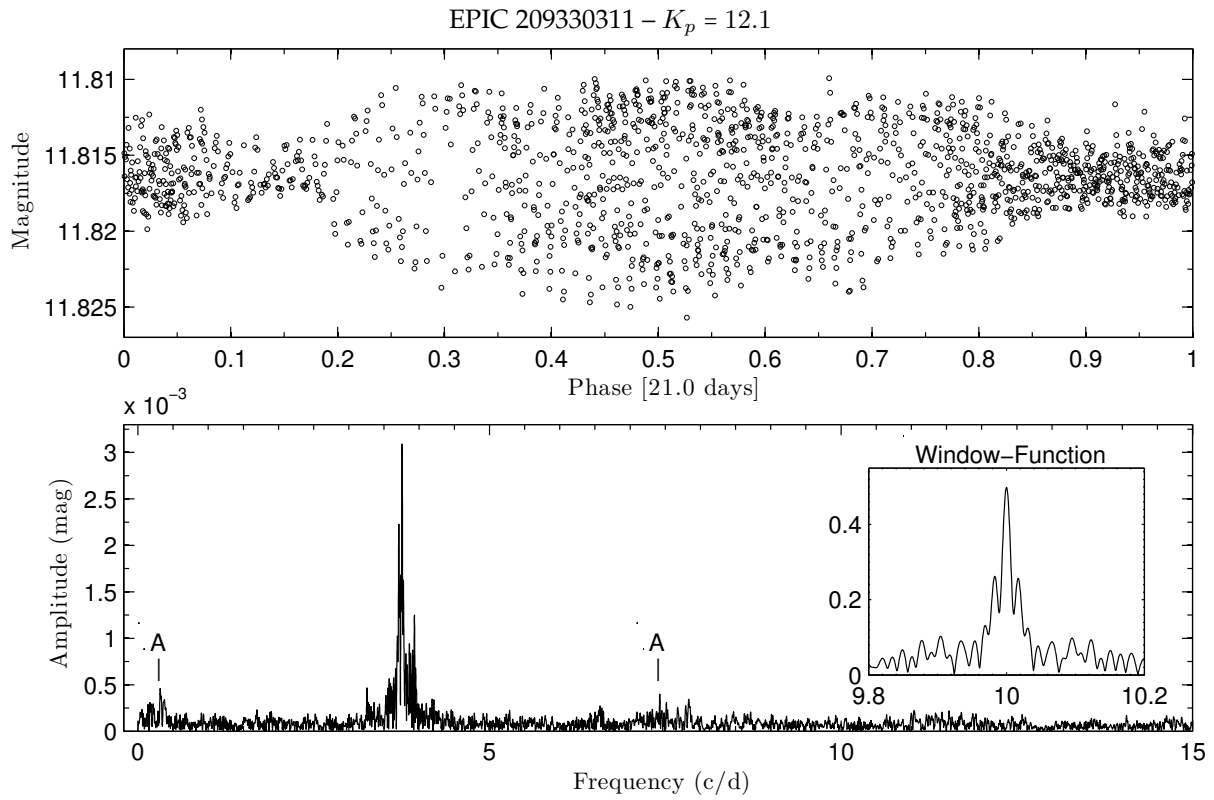


Figure 2.1: This figure illustrates how Fourier analysis in general can be used as a tool in time series analysis – here a Fourier spectrum is shown for a 12th magnitude variable star. The top panel shows the phase folded light curve for the star where several oscillation periods must be present in order to explain the overall form. The bottom panel display the Fourier spectrum of the same star where a signal with a period close to 4 c/d is clearly seen. The right hand subplot in the same panel is the window function and it also shares the same units on the axis as the overall panel. Lastly, alias peaks approximately offset by 4 c/d from the central peak and is labeled as “A”. Their presence is due to the Kepler’s approximate 6-hour drift motion.

However, because time series are discrete in time they cannot be described by a simple Fourier transform and (2.1) does not hold for our analysis. What is needed in time series is a Discrete-Time Fourier Transform (DTFT). The fact that time series are time-sampled rather than continuous means that the Fourier transform entails spectral artifacts into the Fourier spectrum. In other words the data sampling creates a so-called spectral *window function* in the Fourier spectrum. As the window function effectively is the quality limit of the data, from an astronomic point of view the appearance of the window function is first of all determined by the quality of the observations and secondly how the observations are sampled.

Figure 2.1 illustrates how a phase folded time series (top panel) from a most possible multi-periodic variable star looks like when Fourier transformed (bottom panel). Here the window function for our K2 C0 data can be seen in the right hand subplot in the bottom panel. From the bottom panel, a peak at a frequency of about 4 c/d clearly dominates the spectrum, however, we will in Chapter 4 return to how we employed a spectrum like this in this project’s analysis. In the cases where the data is unevenly sampled or when a systematic signal either contained in the data itself or in the way it is sampled (e.g. the day-to-night sampling for ground based observations), the Fourier spectrum will additionally produce spectral artifacts as we in this project will call aliases. The label “A” as seen in the bottom panel of figure 2.1 shows the spectral artifacts of

the K2 data. Here the aliases are a product of Kepler's drift motion of approximately 6 hours which is in correspondence with their offset location of 4 c/d from the central alias peak at 4 c/d.

As mentioned, since the data quality depends on the window function and the window function is determined by the observational limitations, we need to understand how observations behave when Fourier transformed. Observations set limits on the minimum and maximum period detectable, the spectral resolution¹ and the minimum statistically significant amplitude detectable [32]. The three former limitations can be calculated by

$$\nu_{\min} \equiv \frac{2}{\Delta T}, \quad \nu_{Nq} \equiv \frac{1}{2\Delta t}, \quad d\nu = \frac{1}{N\Delta T}, \quad (2.2)$$

where, in our astrophysical analysis, $\Delta T = N\Delta t$ is the time-span of the combined observation with N being the total number of observations and Δt is the time between each individual observation. As can be seen from $d\nu$ in (2.2) the longer the combined observation of the object, the higher the spectral resolution. Beside the fact that ν_{Nq} , the so-called *Nyquist frequency*, defines the highest detectable frequency for a given observation, this frequency is also important because it defines the maximum sampling rate one needs in order to fully describe variations up to ν_{Nq} . Hence, before requesting any observation time, it is crucial to estimate the Nyquist frequency in order to determine if the equipment at the wanted facility is able to detect the signal of interest.

Another application of Fourier analysis is the importance of *noise* determination. In astronomy, photometry is limited by Poisson statistics where the noise level, f_{noise} , is defined as $f_{\text{noise}} = \sqrt{N_\gamma}$ and N_γ is the number of detected photons [6]. This means, even though a high number of photons can ensure a high photometric precision, noise will always be a limitation. Accordingly, this is also true for Fourier analysis. Because $F(\nu)$ assumes that everything contained in a data set is a signal, noise will appear at some level defined by the strength of the true periodic modulations relative to the background noise [32]. The noise level in the Fourier spectrum appears as a dense "forest" of peaks with amplitudes depending on the quality of the data. In the lower panel in figure 2.1 a noise level of about 0.1 mmag is visible. This means that any signal with an amplitude close to or below 0.1 mmag will be indistinguishable from noise and thus cannot be detected by the means of a Fourier analysis.

Exoplanet Transit Science

The major goal in measuring exoplanet eclipses is to determine fundamental astrophysical parameters such as planet radius, R_p , and planet mass, M_p . In this section we will briefly introduce the basics to understand exoplanet transits for then later to use the underlying theoretical foundation to examine this project's discovered exoplanet candidate. In this section all figures and equations are from [8].

¹The accuracy of the period determination.

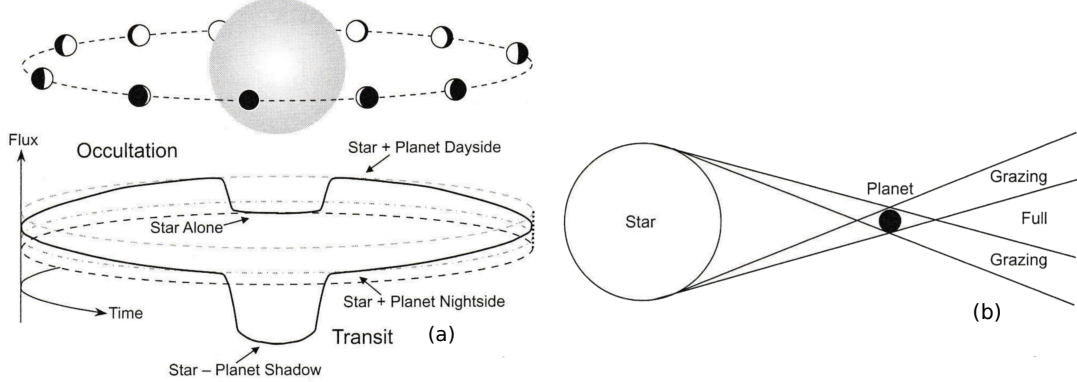


Figure 2.2: This figure shows the basics of exoplanet eclipses: a) shows an illustration of how a full-period light curve of a planetary system will look like as a function of time. b) shows how light from the stellar disk creates full and grazing events.

Geometry

An eclipsing event is when one astronomical object shadows another. For objects of unequal size (which are most frequent) astrophysicists distinguish between *transits* and *occultations* when the full disk of the smaller body pass in front of the larger body and when the smaller body is totally concealed by the larger body, respectively (see figure 2.2a). Furthermore, we distinguish between a *full* and *grazing* event, where the latter is when the stellar and planetary silhouettes are not completely overlapping (see figure 2.2b). As for the duration of transits we will only consider full-events in this project.

In most cases the identification of a transit insures an inclination angle of $i \sim 90^\circ$. However, this is not always true for a planet in a close-in (short period) or highly eccentric ($e \sim 1$) orbit, where i can be substantively lower. To understand a planetary system we need first to describe the geometry of it. Johannes Kepler was the first to ever realize that planetary orbits are elliptic. This means that one can define a star-centered coordinate system (x, y, z) from the minimum and maximum distance from the star to planet, also called *periapse* and *apoapse*, respectively. However, because such a coordinate system is not suited for practical reasons, an easier description of exoplanet dynamics, as seen in figure 2.3a, is a coordinate system centered on the star (X, Y, Z) with Z pointing towards us and X and Y parallel and perpendicular to the planetary orbit, respectively. The two coordinate systems define two planes and the line of intersection is called the *line of nodes*. By this line we define the point where the orbit crosses the (X, Y, Z) coordinate plane moving from below to above the plane, also called the *ascending node* – see figure 2.3a. Now the angle, Ω , between the x -axis and the radius vector to the ascending node can be defined, also called the *longitude of the ascending node*. Lastly, the radius vector to the ascending note and periapse defines the angle, ω , which is called the *argument of periape*.

Having the geometry in place we are now able to understand the dynamics. As seen from figure 2.3b a geometrical important parameter related to i is the sky-projected distance at conjunction (the so called impact parameter) which is given by

$$b = \frac{a \cos(i)}{R_*} \left(\frac{1 - e^2}{1 + e \sin(\omega)} \right), \quad (2.3)$$

where a is the semimajor axis and R_* is the radius of the host star.

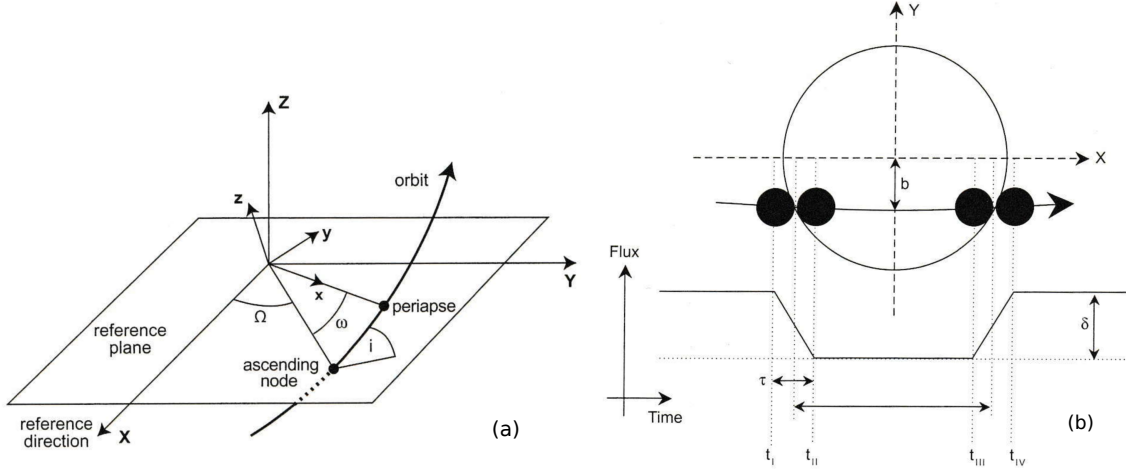


Figure 2.3: This figure shows the basics of exoplanet eclipses: a) shows the relationship between the (x, y, z) (a star-centered coordinate system with respect to apoapse and periapse) and (X, Y, Z) (a star-centered coordinate system respect to the line-of-sight) coordinate systems and the angles i , ω and Ω ; b) illustrates a transit in the (X, Y, Z) coordinate system and a matching light curve. This figure also shows the parameters b , δ and some transit times.

Transit Times

As seen from figure 2.3b we define four transit times (t_I , t_{II} , t_{III} and t_{IV}) belonging to disk-edge-events at ingress and egress. In addition the light curve offers the observables T_{tot} , T_{full} and δ corresponding to the *total* transit time, the time when the *full* planetary disk is within the stellar disk and the so-called transit depth, respectively – see figure 2.3b. The times T_{tot} and T_{full} are given by

$$T_{\pm} = \frac{P}{\pi} \sin^{-1} \left(\frac{R_* \sqrt{(1 \pm \eta)^2 - b^2}}{a \sin(i)} \right) = \begin{cases} T_{\text{tot}} \equiv t_{IV} - t_I, & \text{for (+)} \\ T_{\text{full}} \equiv t_{III} - t_{II}, & \text{for (-)} \end{cases}, \quad (2.4)$$

where $\eta \equiv R_p/R_*$ is an useful definition. Using T_{tot} and T_{full} in the limit $R_p \ll R_* \ll a$ we now have an equation to determine b and an equation to determine a

$$b^2 \approx \frac{(1 - \sqrt{\delta})^2 - (T_{\text{full}}/T_{\text{tot}})^2(1 + \sqrt{\delta})^2}{1 - (T_{\text{full}}/T_{\text{tot}})^2}, \quad (2.5)$$

$$\frac{R_*}{a} \approx \frac{\pi}{2\delta^{1/4}} \frac{\sqrt{T_{\text{tot}}^2 - T_{\text{full}}^2}}{P} \left(\frac{1 + e \sin(\omega)}{\sqrt{1 - e^2}} \right). \quad (2.6)$$

Notice here that (2.5) can be used to solve for i in (2.3) which we will use later.

Absolute Dimensions

As seen in figure 2.2a the light curve of a transiting planet is determined by the combined flux, $F(t)$ from the stellar host and the planet. This means besides transiting events, in time when an increased fraction of the planets dayside comes into view and occasions of occultation, $F(t)$ will increase and decrease, respectively. In addition the stellar flux may vary in time due to rotation, spots, flares etc. (the stellar host may even be a variable star itself). However, for simplicity we will treat the stellar brightness as a constant.

Moreover, usually the flux contribution of the planet is insignificant, meaning only transiting events with a constant out-of-transit flux level are visible in the light curve. With the stated assumptions the maximum loss of light during a transit is given by

$$\delta \approx \eta^2 \equiv \left(\frac{R_p}{R_*} \right)^2. \quad (2.7)$$

Thus, the transit lightcurve only provides the relative radius R_p/R_* . To gain knowledge of the planet's mass, radial velocity measurements of the host star are needed. More specific, the quantity that is required is the radial velocity semiamplitude, K_* , and we can relate this to Kepler's 3. law

$$\frac{M_p}{(M_p + M_*)^{3/2}} = \frac{K_* \sqrt{1 - e^2}}{\sin(i)} \left(\frac{P}{2\pi G} \right)^{1/3}, \quad (2.8)$$

where G is the gravitational constant, M_p is the planet mass and M_* is the mass of the stellar host. However, just as R_p cannot be determined independently of R_* , neither can M_p be determined independently of M_* . Thus, this illustrates the importance of studies such as asteroseismology which are typical used to determine stellar parameters. However, as this project illustrates, other methods to determine stellar parameters can be used under certain circumstances.

Moreover, in situations where R_* , R_p or a are unknowns, the dimensionless ratios R_*/a and R_p/a are in fact still important. This is due to the fact that both R_*/a and R_p/a set the scale for the tidal interactions between the star and planet. Moreover, R_p/a tells how big a fraction of the stellar luminosity the planet is irradiated by and R_*/a is important because it can be used in the following relation which also can be derived from Kepler's 3. law

$$\bar{\rho}_* + \eta^3 \bar{\rho}_p = \frac{3\pi}{GP^2} \left(\frac{a}{R_*} \right)^3. \quad (2.9)$$

Here $\bar{\rho}_*$ and $\bar{\rho}_p$ are the mean density of the host star and planet, respectively. Thus, amazingly a relation for a combination of $\bar{\rho}_*$ and $\bar{\rho}_p$ can be determined without the independently stellar and planetary parameters.

Limb Darkening

As seen from figure 2.3b the transit depth is illustrated to be constant over the transit event. However, when analyzing stellar disks one realizes that real stellar disks are brighter at their centers and fainter at their stellar limb. This effect is called Limb Darkening (LD) and leads to a round-off curvature at the bottom of the transit light curve and blurs the second and third contact point (LD is sketched in figure 2.2a compared to no LD feature in figure 2.3b). Because temperature and opacity² vary with altitude in the stellar atmosphere, an inclined line of sight to the stellar limb means that an optical depth of unity is reached at higher altitudes, thus, accessing to a cooler and less radiation intense region compared to a direct line of sight to the center of the stellar disk. As seen later, LD is an important effect to take into account for transiting signals.

²The transparency of a material.

*“In science, one man’s signal is
another man’s noise”*
– Edward Ng, 1990

3

Data Reduction

From the KASOC database a Barycentric Julian Data (BJD) was already applied to the raw data and, accordingly, throughout this project we will refer times to the epoch of BJD-2454833 corresponding to the start of the *K2* mission.

Data Exclusion

The C0 data compared to later campaigns are displaying large photometric scatter, especially the first part of the data. In addition, the spacecraft was in safe modes approximately between the times 1899.3-1902.5 and 1909.1-1935.9 for correction of altitude errors (see voids in figure 3.3a). These and some numerous single images was tagged for each TPF by the Kepler pipeline as having a bad quality. These so-called KASOC_FLAGS can be seen in table A.2 and only frames with a bit value of 0 were used, corresponding to images who did not suffer from cosmic rays, detector glitches and pointing adjustments. Figure 3.1 shows the effect of the pointing jitter. Because customized aperture masks were selected from a summed image¹, such images were crucial to exclude beforehand. The exclusion of images varied from TPF to TPF, however, approximately 46% of the total data for each TPF (including the save modes) was excluded at this point.

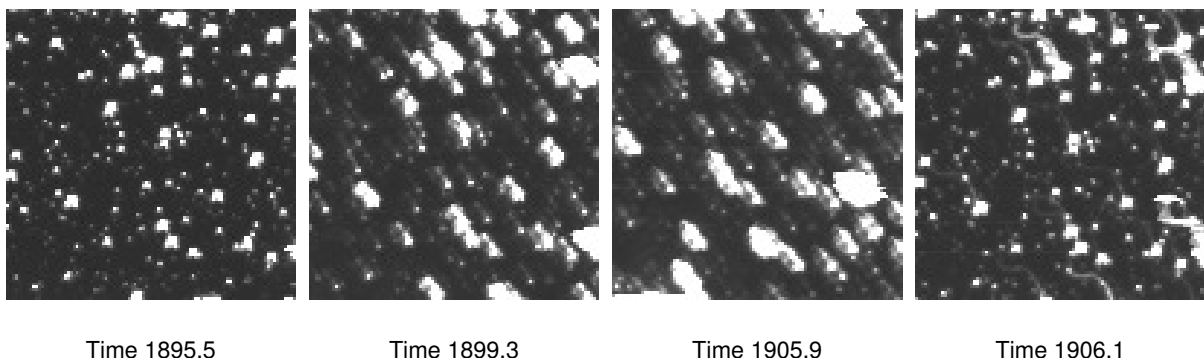


Figure 3.1: This figure displays four single $6.6' \times 6.6'$ FOV images of the same central region of M35 at four different times. The far left image displays a frame with a good quality, while a large jitter clearly can be recognized in the three most far right images, due to spacecraft pointing instability or thruster firing events. Thus, these and similar images are excluded before further analysis. Associated observation times are represented below each image.

¹Simply meaning that each flux value of each image pixel was additively combined for each TPF.

3.2 APERTURE PHOTOMETRY

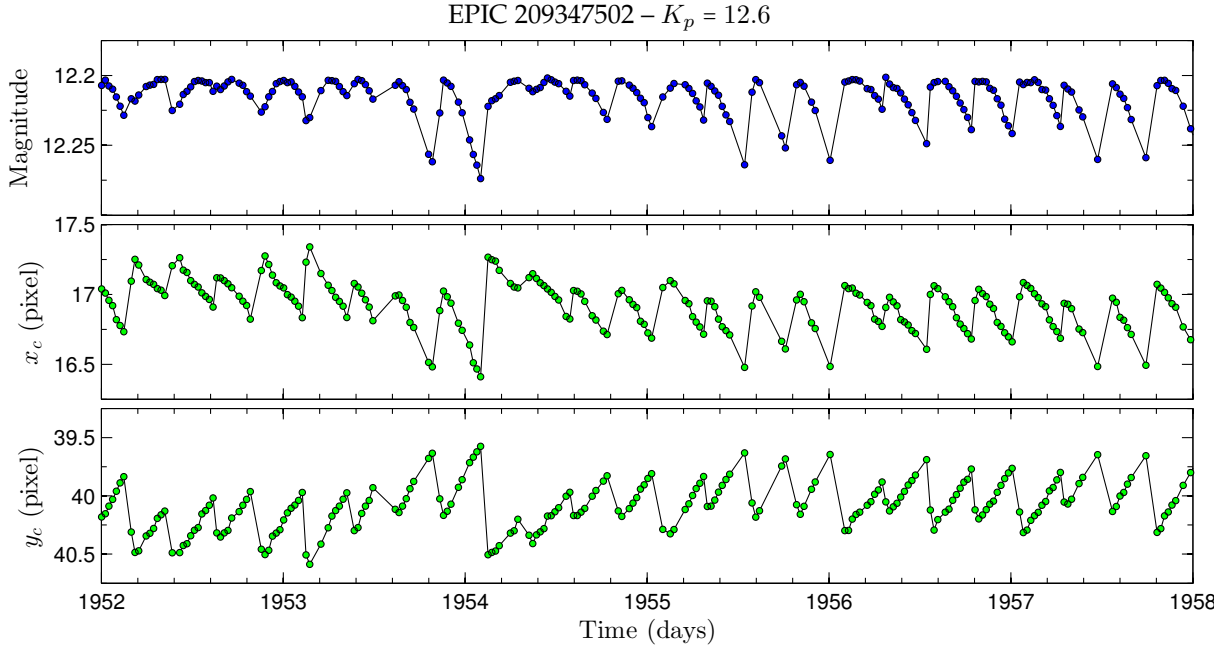


Figure 3.2: This figure displays; top panel: the magnitude extracted from raw photometry for a star with $K_p = 12.6$; mid and bottom panel: the centroid positions x_c and y_c calculated by the COF for the same star. The figure serves to illustrate how the pointing instability of Kepler effects the raw photometry. Notice that Matlab assigns image coordinates after rows and columns, hence the reversed vertical axis in the bottom panel.

In continuation, points *near* thruster firing events was also cut out of the final data pipeline, however, to designate these needs a more detailed analysis and therefore this was done with an automated preparation pipeline designed for Kepler and K2 time series [12]. In section 3.3 we will return to this subject of study.

Aperture Photometry

In this project a large number of related articles have been a great source of inspiration for the computational work of extracting time series from the extremely stellar crowded FOV such as M35 and NGC 2158. Our own preparation routine is in short designed to make aperture photometry with 4 different masks (a circular, elliptic, squared and customized) both with a *local* and a *global* background subtraction. In this section, we describe these computational methods.

Because the horizontal and vertical flux centroid positions of a given star were needed for the later automated data preparation, we started out by finding the so-called Center Of Flux (COF) in the science frames. If we denote f_i as the flux belonging to the i 'th pixel and $\sum_i f_i$ as the total flux of the star, the centroid pixel position in the horizontal and vertical direction of an image is given by

$$x_c = \frac{\sum_i f_i x_i}{\sum_i f_i}, \quad y_c = \frac{\sum_i f_i y_i}{\sum_i f_i}. \quad (3.1)$$

When estimating the COF for a certain star, a squared aperture was used so the star was totally contained in the aperture. Both the aperture size and number of pixels used to calculate the COF were correlated to the so-called *Kepler magnitude*, K_p , of the target star. For stars with $K_p = (10-12, 12-14, 14-17)$ an aperture mask of $(9 \times 9, 7 \times 7, 5 \times 5)$ pixels

3.2 APERTURE PHOTOMETRY

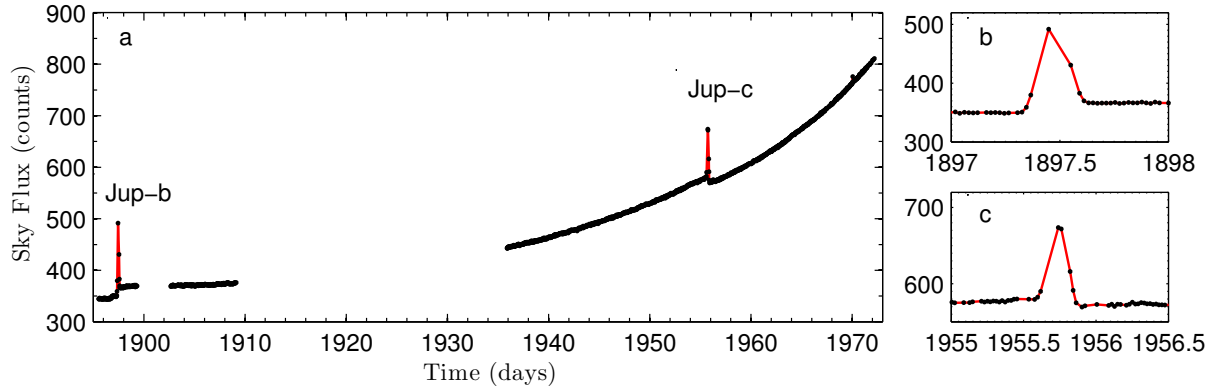


Figure 3.3: This figure shows the sky background flux as a function of time for C0. Here a) clearly demonstrates how the flux increases with time and the above mentioned save mode events are clear to be seen as the two voids. In the same panel two large peaks labeled Jup-b and Jup-c are results of reflected light from Jupiter. A zoom-in on peak Jup-b and Jup-c can be seen in panel b and c, respectively. All data with quality flags corresponding to any sort of contamination have been excluded and are not shown.

and number of used pixels (15, 10, 5) were used in (3.1), respectively. However, even though the limited aperture and position pixels were used to avoid flux contribution effects from stellar crowding, the two parameters were selected manually for blended stars. The centroid positions and the raw photometric light curve for a star with $K_p = 12.6$ can be seen in figure 3.2. The effect of Kepler's 6 hours drift and associated thruster firing events is clearly visible from the zigzag behavior of x_c and y_c . The figure illustrates how the largest shifts in centroid positions give the largest magnitude drop (see upper panel). Thus, artifacts from changing stellar positions must be corrected for in order to obtain a higher photometric precision.

Another consequence of the K2 mission is the fact that the sky background flux level increases gradually as the angle between the Sun and Kepler's boresight slowly decreases during mission campaigns – this is shown in figure 3.3. In addition, the varying angle between Kepler and the Sun results in a heating of the telescope and a change in focus [12]. These effects have not been taking into account in the raw data, thus, a robust background flux subtraction is needed. We start by describing how a global TPF background flux is found².

As mentioned in the last Chapter 1, our data consists of 154 TPFs with a dimension of 50×50 pixels with varying images per stamp. For each TPF analyzed in this project a median flux value of 10 pixels distributed more or less randomly across the target pixel data was first selected as the sky background level for each image. However, this technique introduced a very high background scatter (and often drowned the signal of variability) which may be explained by the read-out technique of Kepler's CCDs where trails of bright stars can induce noise to background pixels. Instead, from a summed image each of the 2500 pixels (from the 50×50 pixels frames) was ranked after received counts. Secondly, from a sample of 500 pixels, which have the lowest flux count, a polynomial function of the order of 10 was fitted to the increasing trend of the background flux for each pixel between the times 1936-1954 (see figure 3.3). A selection of 50 pixels having the lowest standard deviation from the fit were chosen as good reliable background pixels and, lastly, the median of these was calculated and used to correct for the brightness increase of about 30% over the course of C0. The

²For a more comprehensive background flux correction see how Lund & Handberg [17] have implemented Scott's rule [27].

3.2 APERTURE PHOTOMETRY

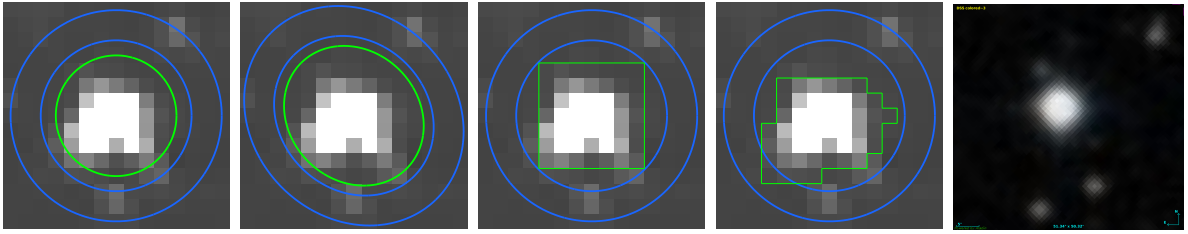


Figure 3.4: This figure illustrates how aperture masks (green masks) and local background fluxes (blue bands) were constructed at pixel level. Seen from the left, the first four images display the circular, elliptical, squared and customized aperture, whereas the picture to the right is a DSS image from the CDS server (see <http://cds.u-strasbg.fr/>) covering approximately the same about $1' \times 1'$ FOV.

median flux rather than mean flux was used because of the robustness due to cosmic ray contamination. Moreover, notice that the global background technique assumes a uniform background flux across a given image, which may be a bad approximation for the two encountered events of reflected light from Jupiter. In figure 3.3a these events are labeled as Jup-b and Jup-c and a zoom-in of these approximately 12 hours contaminations can be seen in panel b and c, respectively.

In defining aperture masks we constructed a circular, elliptical, squared and customized pixel mask to test how each collaborated with the large plate scale, the regular drift movement of Kepler and crowding in our data. An illustration how these pixel masks look like for a $K_p = 12.1$ star with multiple nearby stars can be seen in figure 3.4. The two blue circles/ellipses enclose the so-called local background, whereas the green masks are used as apertures. As seen from the same figure, the local sky background flux was estimated with a circular band for the circular, squared and customized aperture, and an elliptical band for the mask of the ellipse. Both for the aperture masks and background bands, only pixels that were totally enclosed by the representative mask/background band were used for photometry. Defining the circular, elliptic and squared aperture was done in a general way, however, the elliptical mask's major axis was orientated in the approximately direction of the spacecrafts drift motion, hence, withholding more flux from the star. Notice that in figure 3.4 the elongation of the customized apertures almost is perpendicular to the elliptical mask which is only specific to this target.

On the other hand the customized apertures were created with more care for blended stars, as can be seen in the two most far right images in figure 3.4. In the far most right DSS image 4 visually close-by stars can be seen, where 2 of these are almost totally contaminating the target star of the K2 data. In the following the Signal-to-Noise Ratio (SNR) was a very useful tool for constructing the customized aperture. Because the arrival of photons is described by Poisson statistic the SNR can be calculated by [6]

$$\text{SNR} = \frac{Sg}{\sqrt{Sg + Ng + r^2}}, \quad (3.2)$$

where S is the total flux from the star, N is the background flux, g is the gain of the camera and r is the read-of-noise of the CCDs. For Kepler these are $g = 117.02 \text{ e}^-/\text{ADU}$ and $r = 96.284056 \text{ e}^-$ and S and N are measured in received counts or e^- [6]. The customized aperture mask was created as following: first of all from a summed image all pixels with a $\text{SNR} \geq 15$ were found, where the global rather than the local background flux was used due to its generally higher result for the SNR. Secondly, by visually inspecting a higher resolution image from the DSS, SDSS or 2MASS catalog, crowding near the target star

3.3 AUTOMATED PREPARATION PIPELINE

could be estimated. In the case of blended stars the so-called *watershed* method [3] was manually performed. In short this technique deals with locating lines between regions that can be seen as topographical surfaces and, thus, efficiently distinguishing between blended stars³.

After defining aperture the photometry was done with the local and global background flux resulting in 8 different light curves. Every light curve in this project is represented with a magnitude scale instead of flux, and the conversion is given by

$$m = -2.5 \log(f) + k, \quad (3.3)$$

where f denotes the flux of object in the unit of counts/ADU and $k = 25$ is a correction constant which is not particular important because only a relative magnitude is needed for our analysis. As a final step, by visually choosing the light curve displaying the largest signal and smallest scatter, this light curve was selected for a final automated preparation pipeline, namely, a fusion between Handbergs & Lunds pipeline for the Kepler mission [12] and K2 mission [17].

Automated Preparation Pipeline

One of KASOC's main tasks is to provide asteroseismic analyses of Kepler Objects of Interest (KIC). Hence, the automated preparation pipeline (also called the *KASOC filter*) [12] was first of all developed to remove signals that could prevent these asteroseismic analyses, which planets and instrumental effects produce. Because the Nyquist frequency for the SC and LC data is high enough for the detection of solar-like oscillations in main sequence stars and for studies of evolved red giant stars, respectively, the KASOC filter serves as an important tool for the community. Besides the efficient correction for instrumental and planetary signals, because the eclipse signature of EBs are comparable to those of exoplanets, the KASOC pipeline is also suited for EB studies. Moreover, the pipeline K2P² was later developed for the K2 mission, however, only a small part of this pipeline is added to the KASOC filter as seen later. We will call the combined Automated Preparation Pipeline for APP.

The KASOC filter is not based on any models, hence, it solely uses technical/computational algorithms. The constituents of the filter are based on the following sub-filters⁴

x_{jump} filter that corrects for flux-jumps between campaigns.

x_{long} filter that removes long-term instrumental or stellar variability effects.

x_{transit} filter that removes known planetary transits.

x_{short} filter that removes unknown planetary transits.

x_{pos} filter that removes short-term instrumental effects.

The asteroseismic analysis is not in our interest, however, exoplanets and variable stars are. Thus, we have the two following filters

$$\text{Filter}_1 = x_{\text{jump}} + x_{\text{long}} + x_{\text{transit}} + x_{\text{short}} + x_{\text{pos}}, \quad (3.4)$$

$$\text{Filter}_2 = x_{\text{jump}} + x_{\text{long}} + x_{\text{pos}}, \quad (3.5)$$

³For automated implementation of the *watershed* algorithm see [17].

⁴The names of the filter constituents are adopted from the original paper [12], except for x_{jump} .

3.3 AUTOMATED PREPARATION PIPELINE

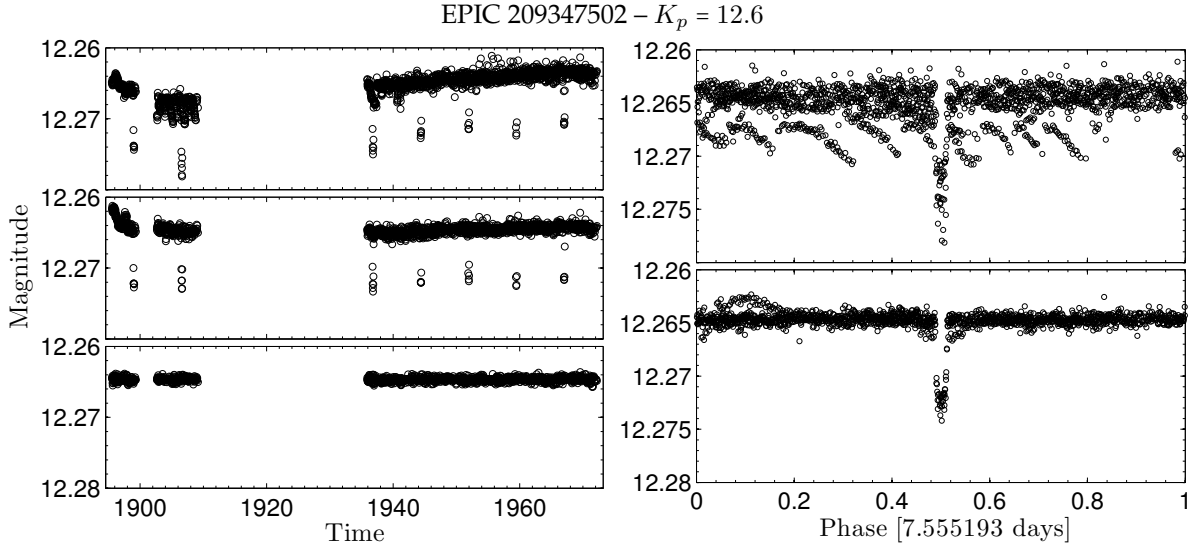


Figure 3.5: These figures illustrate how the APP generates much cleaner light curves for the exoplanet candidate EPIC 209347502. Left figure displays the light curve – top panel: own extracted light curve (no filter); mid panel: corrected light curve after Filter₂ was used; bottom panel: all signals are extracted by Filter₁. The right hand figure is a phase curve of the two upper left panels.

where Filter₁ removes any signal of variability as well as instrumental effects and Filter₂ removes only instrumental effect.

The primary attribution for flux changes between observation campaigns is the sensitivity variations between the CCDs upon which a given star falls. Also, the changing pixel-level sensitivity can change stellar crowding, hence, contributing to the flux variations. The x_{jump} filter corrects for these effects which are caused by the roll motion of the spacecraft between campaigns. Because the C0 data contains 2 save mode events (thus leaving 2 gaps in the observations) this campaign has effectively 3 coherent observations. From the data analysis of the light curves it was evident that the brightness level of these 3 observations rarely was coincident. Because x_{jump} is based on 2 algorithms⁵ which works best for levels of constant brightness, we should not expect significant improvement on flux-jumps in our C0 data. The filter x_{long} depends on the tunable timescale parameter τ_{long} and essentially any periodicity with a period below τ_{long} will be removed. In addition to the unknown planetary transits the x_{short} filter also removes any sharp feature not accounted for previously. x_{short} as well depend on a tunable timescale parameter τ_{short} which sets the timescale this filter should look for sharp features.

Lastly, from the pipeline K2P² the filter x_{pos} corrects for the photometric variability caused by the motion of the spacecraft (which mostly is dominated by the 6 hours variability – see figure 3.2). x_{pos} makes a 1D correlation between the flux variation and the stellar position on the CCD as found by (3.1). In short, the correction was done by first calculating the curve length, s , along the trend that arises from a y_c vs. x_c plot. Secondly, by plotting a filtered photometry vs. s ,⁶ data points near thruster firing events can be recognized as outliers and are thus excluded. Moreover, the combined trend of this figure reveals the average positional dependency of the flux level which is used as the filter correction.

⁵ x_{long} first estimate the linear trend by a LOcally WEighted Scatter-plot Smoothing (LOWESS) following by a Theil-Sen median slope estimation [12].

⁶For an illustration of this plot see figure 4 in [34].

3.3 AUTOMATED PREPARATION PIPELINE

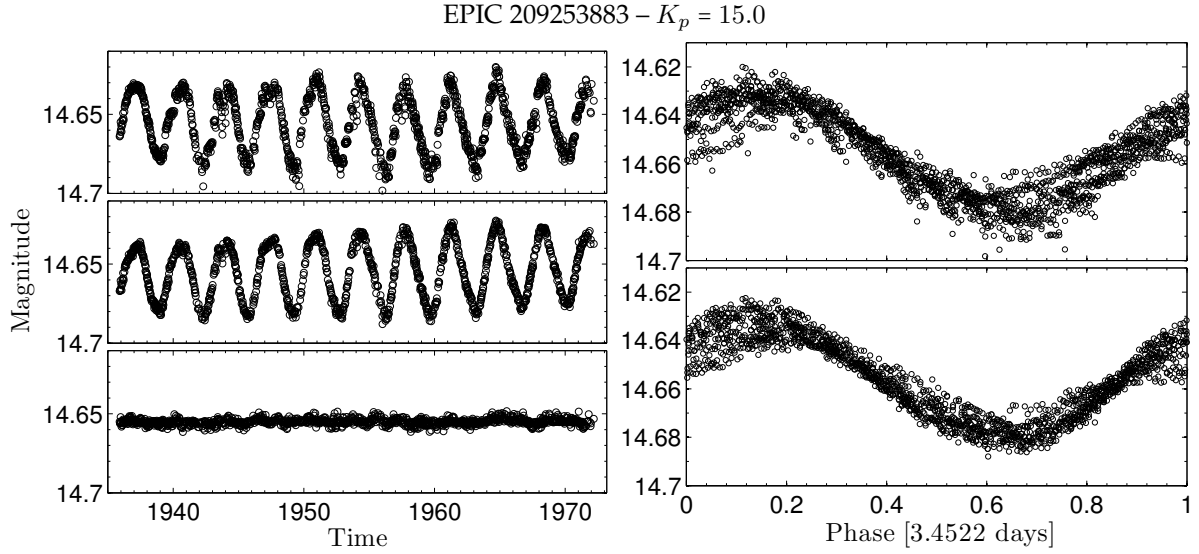


Figure 3.6: These figures illustrate how the APP generates much cleaner light curves for the star EPIC 209253883. This variable star was discovered by Nardiello et al. [22] who suggests that it is a rotational variable. Otherwise, the figure is alike to figure 3.5.

Figure 3.5 illustrates how the APP provides a much cleaner light curve for the exoplanet candidate system EPIC 209347502. A normal plus the phase folded time series are displayed in the left and right hand figure, respectively. The left panels from the top shows the raw, Filter₁- and Filter₂-corrected time series, respectively. From this figure it is evident that x_{jump} partly corrects for the brightness levels. Moreover, the bottom panel clearly illustrates the efficient removal of the exoplanet transits due to the filters x_{transit} and x_{short} . The phase folded light curves (right hand figure) emphasizes the improvement from the raw time series to the APP corrected time series. Here the two right hand panels are just phase folded light curves of the two upper left panels. A further illustration can be seen in figure 3.6, where only the last coherent observation (the most stable one) is plotted so more details are visible. This figure shows the APP's ability to work with multi periodic variable stars, where the multi periodicity most clearly can be seen by the broadness of the phased light curve.

"Two possibilities exist: either we are alone in the Universe or we are not. Both are equally terrifying."

– Arthur C. Clarke, 1999

4

Results and Analysis

Photometric Precision

The photometric precision for the original Kepler mission was often stated to be about 22 ppm over a 6 hour window for 11th-12th magnitude dwarf stars [10] and as low as 10 ppm for 10th magnitude stars [24]. In Vanderburg & Johnson's study [34] they showed that regarding 11th-12th magnitude stars, the photometric precision for the K2 mission increased to about 163 ppm. However, by the same computationally principles as this project takes advantage of, they could extract photometry with a precision of about 33 ppm. In this project we do not expect to obtain a 33 ppm photometric precision, first of all due to stellar contamination and secondly because our aperture mask selection technique is not perfect.

The standard deviation from the APP routine was estimated by calculating the Median Absolute Deviation (MAD) of the time series and then scaling it to yield the standard deviation of the long timescale, τ_{long} . Hereafter, $\sigma(t)$ was divided into 6-hour bins, where the median was used to yield σ for each star. Finally, the photometric precision for each star was divided into integer intervals after K_p , where the median for

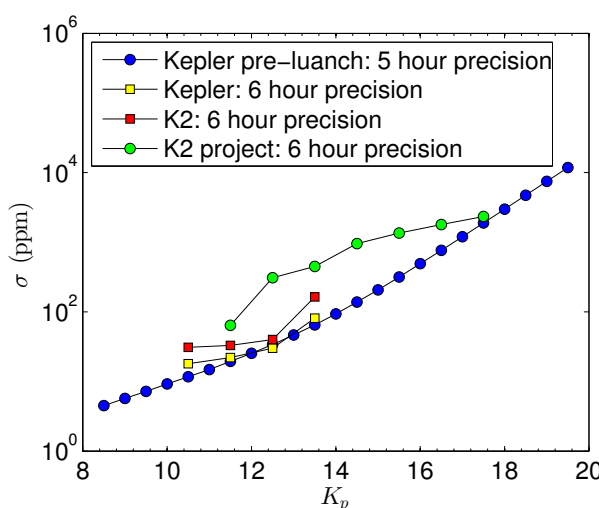


Table 4.1: MEDIAN PHOTOMETRIC PRECISION

K_p	Kepler Prediction 5 hour (ppm)	Kepler From [34] 6 hour (ppm)	K2 From [34] 6 hour (ppm)	K2 APP (ppm)
10-11	12	18	31	
11-12	19	22	33	64
12-13	34	30	40	309
13-14	65			450
14-15	138	81	164	955
15-16	317			1355
16-17	766			3368

Figure 4.1: This figure displays the photometric precision as a function of Kepler-magnitude. The blue symbols are 5 hour pre-launch predictions for the Kepler mission, found at <http://keplerscience.arc.nasa.gov/>; the yellow and red squared symbols are 6 hour photometric results from Vanderburg et al. [34] for the Kepler and K2 mission, respectively; the green symbols are photometric precisions for the Kepler mission found in this project. All plotted data can be seen in table 4.1.

4.2 MAIN-BELT ASTEROIDS

each interval was estimated. Table 4.1 shows the pre-launch predictions for Kepler’s photometric precision for a 5 hour window, as well as the median photometric precision estimated by [34] both for the Kepler and the K2 mission for a 6 hour window and results of this project for a 6 hour window for the Kepler mission. Moreover, these results are also displayed in figure 4.1. As expected, both table 4.1 and figure 4.1 clearly illustrate that this project’s photometric precision, compared to that of the original Kepler mission, is off by several factors, here with a lower limit of 64 ppm (about a factor of 3 from the Kepler mission’s pre-launch predictions) for 11th-12th magnitude stars. Lund & Handberg [17] found that it in general, when the amplitude of the underlying stellar signal dominates the variations, such as many Classical pulsators, the correction of the instrumental signal made by the APP is less effective. This means that a higher photometric precision could be obtained if only stars showing minimal variability were used in the test of the photometric precision.

Also, the trend of our estimated photometric precision in figure 4.1 (green symbols) surprisingly seems to counterbalance the trend of the pre-launch predictions (blue symbols) instead of following it. Moreover, our data also indicates a lower photometric precision for faint stars (of 17th magnitude) than one would expect from the pre-launch predictions. Our stellar sample mainly consists of stars with a magnitude between 12-15 (owing to selection criteria and the cluster’s high frequency of stellar objects in this magnitude range) and consists of only about 50 stars. Thus, this trend could be suspected only to reflect these effects, however, as our results display no clear scatter the trend must be real. If this is true an extrapolation of the trend may reveal that a higher photometric precision can be obtained with the K2 mission than expected, hence, this suggests the presence of new unknown complications of the data. Thus, as one can exploit this effect when analyzing faint stars, this would be a motivating future project to analyze.

Main-Belt Asteroids

Due to the K2 mission’s observed fields along the ecliptic plane a large number of asteroids are present in the data. A search for these asteroids was done by Szabó et al. [31] earlier in 2015 and they suggest that the majority should be main-belt asteroids (most possibly belonging to the Kuiper-belt located between Mars and Jupiter). The large plate scale of Kepler’s CCDs means an increasing probability for asteroids to contaminate the photometry compared to traditional CCDs used for high-precision photometry (typically with a plate scale of 0.1''-0.5''/pixel [31]). Thus, for the future of the K2 mission one would first of all like to know the effects of asteroid contamination on the photometric precession and secondly how to take these events into account.

Szabó’s team showed that, from a sub-sample of 300 stars in the 9 days K2 Engineering-2 Test (E2) data, 147 stars suffered from asteroid encounters and many of these stars even suffered from multiple encounters. Here an “encounter” is when an asteroid crosses the photometric aperture of a star. A large number actually enters the stellar PFS, whereas the probability for an asteroid to totally contaminate the stellar disk is extremely low. Featured as a brightness increase in the light curves Szabó et al. suggest that the asteroids seen in the K2 data will have an absolute magnitude in the range 18-21.7. However, due to the much higher stellar density for our FOV compared to that analyzed by Szabó et al. there should be a much higher probability of asteroid contamination.

4.2 MAIN-BELT ASTEROIDS

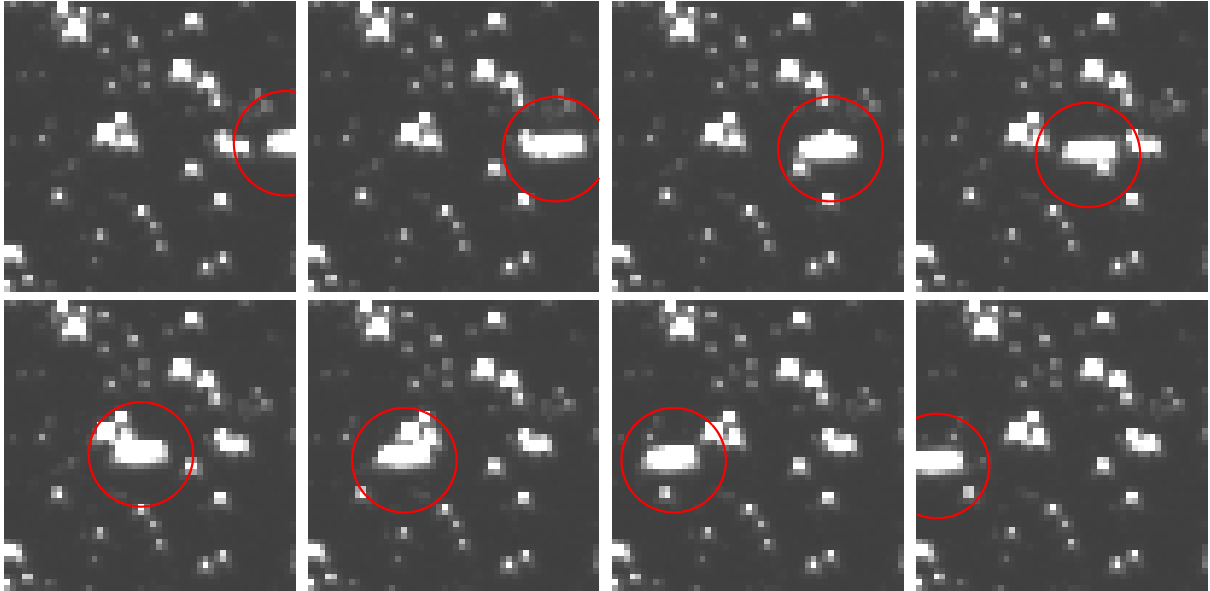


Figure 4.2: This figure shows a large asteroid contaminating several stars in this $10' \times 10'$ FOV. The red circles enclose the largest observed asteroid in a sequence of 8 images going from upper left corner down to the bottom right corner.

In this section we have adopted Szabó et al.'s simple method of asteroid identification; from each of the 154 TPF a short animation was made and inspected visually for asteroid contamination. Figure 4.2 shows a small time-sequence of an animation from multiple combined picture-stamps located at the top edge of M35. Here the red circles enclose the biggest asteroid observed. By the simple visual inspection, about 263 stars with a magnitude < 15 suffered from asteroid contamination (and a much higher encounter frequency for stars with magnitude > 15). In addition we counted asteroids present in stamps belonging to the first left vertical column and bottom horizontal row. Because the path of main-belt asteroids over the combined image of the two stellar clusters approximately was going from the upper right corner to the lower left corner (corresponding to the overall motion of the Kuiper-belt) – see figure 1.1 – these selected TPFs work like a net catching most asteroids. Though, there is a detection bias. This is first of all due to the facts that some asteroids enter the image too late to be detected, secondly some asteroids will pass through the image during the extended safe-mode periods and thirdly asteroids that do not belong to the Kuiper-belt may have other trajectories. In all three cases the asteroids may not be detected. From the visual inspection 20 asteroids were found which is a lower limit for our small data selection of C0.

Thus, as Szabó et al. suggested, this project confirms that asteroid contamination can be a problem for high precession photometry and will be relevant in the future K2 mission and other space missions, such as the Transiting Exoplanet Survey Satellite (TESS) [26] and PLAnetary Transits and Oscillations of stars (PLATO) [11]. However, since the x_{short} filter in the APP corrects for sharp features in the light curve, in this project asteroid contamination should pose a minor problem.

4.3 VARIABLE FINDINGS

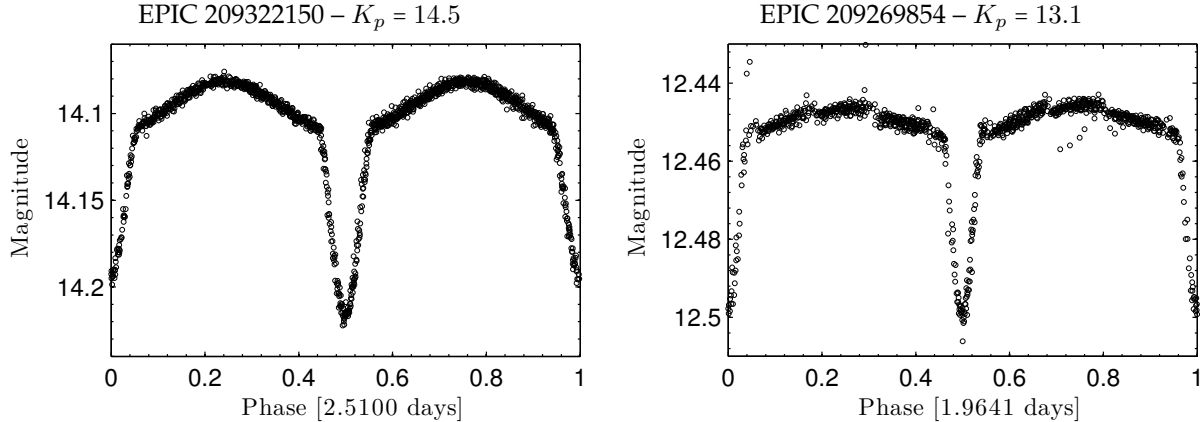


Figure 4.3: This figure shows two phase folded light curves of two eclipsing binary systems which are products of this project. Both systems were initially found by Nardiello et al. [22], hence, we used them to test the functionality of our photometric routine.

Variable Findings

As this project started there was no guarantee that our photometric algorithms would overcome the difficulties associated with the K2 C0 data. However, with the highest precision of 64 ppm for 11th-12th magnitude stars our photometric routine stands the test of our expectations. Originally we started by testing our photometry on already known variable stars from Nardiello et. al.'s catalog [22]. The very first examined candidates were the two Eclipsing Binary (EB) systems EPIC 209322150 and EPIC 208269854 due to the fact that the primary and secondary eclipse have a depth of almost 0.1 mag and 0.05 mag, respectively, which should be easy to detect. Figure 4.3 displays the phase folded light curves of these EB systems. The figure clearly illustrates the functionality of our developed routine. Thus, we started to analyze stars located more or less randomly over the field of the stellar cluster M35 and occasionally variable stars from Nardiello et al.'s catalog. Due to the limited time we did not go into any physical analysis of the variable findings, though with the exception of the exoplanet candidate as we will return to in the next section.

In Chapter 2 we discussed how the theoretical foundation of a Fourier spectrum can be used in a time series analysis. For the purpose of this project we used the very user-friendly program Period04 to merely extract the pulsation period(s) from the analyzed stars. As already mentioned, the Fourier analysis, as any other analytical tools, has constraints relative to the information one can extract. Because C0 has a time span of $\Delta T = 76.7$ days the maximum period detectable of a variable signal is thus 76.7 days, since the signal should recover at least 1 complete cycle. However, with only 1 complete cycle we are not able to conclude that the signal is truly periodic, hence, a more reliable limit is $\Delta T/2 = 38.3$ days because 2 complete cycles can be detected and compared. With the long cadence data of Kepler the minimum period detectable ("the Nyquist period") must be twice the sampling period $2\Delta t = 58.8$ min, since one potentially can detect the maximum and minimum of each cycle. Because Period04 works with cycles/day (c/d) we transform the two above given limits by simply taking the inverse of each, hence, $\nu_{\min} = 0.026$ c/d and $\nu_{Nq} = 24.3$ c/d, where the conservation unit is 1 Hz = 86400 c/d. Also, a signal can only be detected if the spectral resolution of the Fourier transform is $d\nu = 1/(N\Delta T)$. For our data the resolution is $d\nu = 0.013$ c/d. With these limitations and noise prospects in mind we could in many cases extract the period of variability.

4.3 VARIABLE FINDINGS

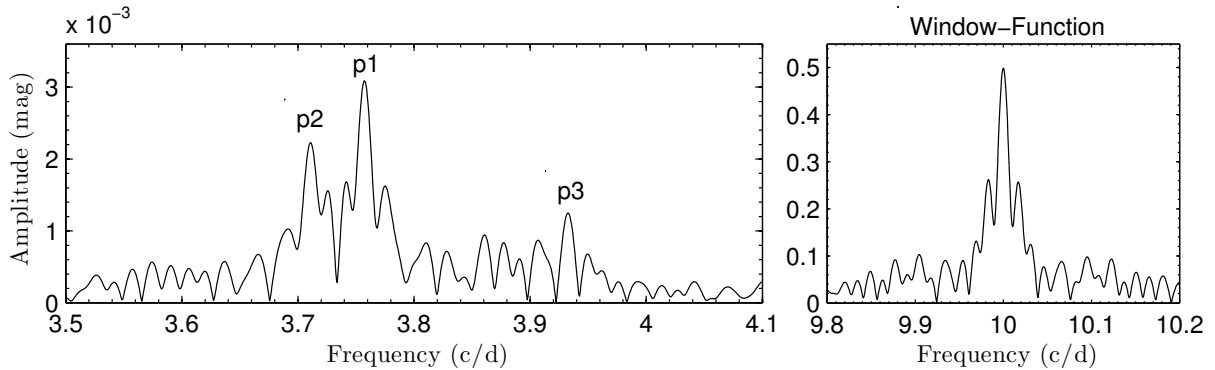


Figure 4.4: This figure is a zoom-in on the dominant frequency peaks in the Fourier spectrum displayed in the bottom panel of figure 2.1. The left panel shows the Fourier spectrum and the right panel displays the spectral window function. The 3 most dominate peaks are labeled p_1 , p_2 and p_3 ordered after peak amplitude where p_1 is the highest.

As an example an illustration of a Fourier spectrum for a $K_p = 12.1$ variable star was given in the lower panel of figure 2.1. The spectrum is clearly dominated by a frequency peak at around 4 c/d. A zoom-in on this dominant peak can be seen in the left panel of figure 4.4, which reveals 3 dominant frequency peaks each with a $\text{SNR} > 5$. The peaks as seen in the figure is labeled p_1 , p_2 and p_3 ordered after peak amplitude where p_1 is the highest. Since only p_1 and p_2 resemble the window function (see right hand panel of figure 4.4) p_3 is not fully resolved to ultimately be trusted. However, the period of p_3 is about 6.1 hours which exactly matches Kepler's drift motion, thus, we can conclude that p_3 is an alias and are not due to a variable signal of the star. Having p_1 and p_2 at a frequency of $\nu_1 = 3.76$ c/d and $\nu_2 = 3.71$ c/d, respectively, is evidence for a multi period variable star. As the light curve of this star (see top panel in figure 2.1) additionally seems to display a long term period, this system may harbor an complex connection between the stellar signals of variability. However, notice that the long term period of 21 days could not be recognized from figure 2.1 which could be due to the fact that the observation gaps in the C0 data reduce the spectral resolution meaning that the signal may be lost in noise. For all variable findings a similar analysis was made.

Due to the limited time, only approximately 50 stars were analyzed in total out of which 16 were already known variables. However, from our small sample we identified 20 new variable stars (although some needs to be followed-up by additional observations for a complete confirmation). All new variables were cross-matched against variable stars in CDS's catalogs within $10''$ from the Ra and Dec found from MAST. Other catalogs rendered were the Two Micron Sky Survey (2MASS), Asiago Pathfinder for HARPS-N (APHN) [22], Exoplanets & Stellar Populations Group¹ [22], K2 Cgampaign 0 Data², K2 Variable Star Catalogue³ [1] and LaCourse et al.'s paper [16]. The information for all new and already known variable findings is represented in Appendix C.1. In addition the light curves of the total 36 variable stars analyzed in this project are displayed in Appendix C.2.

¹<http://groups.dfa.unipd.it/ESPG/varM35NGC2158.html>

²<https://www.cfa.harvard.edu/~avanderb/allk2c0obs.html>

³<http://deneb.astro.warwick.ac.uk/phrlbj/k2varcat/>

4.4 STELLAR SCIENCE OF HOST STAR

Table 4.2: CALIBRATED MAGNITUDES - HOST STAR

$UBVR_cI_c$ System	Value	$ugriz$ System	Value
B	13.001 ± 0.014	g	12.769 ± 0.040
V	12.645 ± 0.011		
R_c	12.422 ± 0.010	r	12.495 ± 0.030
I_c	12.139 ± 0.010	i	12.654 ± 0.440

Table 4.3: DATA OF M35

Parameter	Value	Ref.
d	732 ± 145	[20]
BC	0.028	[9]
$E(B - V)$	0.255 ± 0.024	[30]
[Fe/H]	-0.143 ± 0.014	[29]

The $UBVR_cI_c$ filter system is from Vizier at CDS, and the $ugriz$ filter system is found from the EPIC.

Stellar Science of Host Star

As an exoplanet candidate was independently discovered from our photometric analysis, we dedicate a central part of this project to confirm the planet and estimate the parameters of this object. However, an astrophysical saying is “the better you know your star, the more you can tell about your planet”, hence, we start with describing a technique of estimating stellar parameters. In addition the main benefits of discovering planets orbiting stellar cluster members is first of all that cluster stars are located approximately at the same distance and secondly because stellar cluster parameters are often known from previous studies. In our case, the host star may be a firm member of the stellar cluster M35 and this is for the benefit of our study.

Host Star Membership

Today only a handful of planets have been discovered around stars in stellar clusters. The limited detection of planets was for a long time believed to agree with the difficulties of planet formation in stellar clusters’ severe conditions (e.g. due to the high frequency of stellar encounters and much larger radiation field compared to interstellar field stars). However, new discoveries⁴ of planets in stellar clusters have opened a debate of planetary formation – on top of it all the theoretical foundation still to date cannot fully explain how planets form [33]. Questions such as how the formation process, the frequency and the evolution of planetary systems are with respect to field stars, are fundamental to planetary science, however, even though we will not try to answer these questions, this project’s analysis of an exoplanet candidate may help such studies.

We have tried to determine the membership likelihood to M35 of the stellar host to the exoplanet candidate, by plotting it in a Color-Magnitude Diagram (CMD). However, in order to do so we need first to introduce some concepts. In general when estimating true stellar parameters scattered light has to be taken into account for the true color ($C_1 - C_2)_0$. This is done by

$$C \equiv (C_1 - C_2)_0 = (C_1 - C_2) - E(C_1 - C_2), \quad (4.1)$$

where the color reddening can be estimated by

$$E(C_1 - C_2) = A_1 - A_2 = \kappa E(B - V). \quad (4.2)$$

Here C_1 and C_2 are the apparent magnitude in two observed filters, A_1 and A_2 are the extinction in the two observed filters and κ is a transformation constant depending on

⁴E.g. the confirmation of 3 planets around a stellar member of the open cluster M67 in 2014 [7].

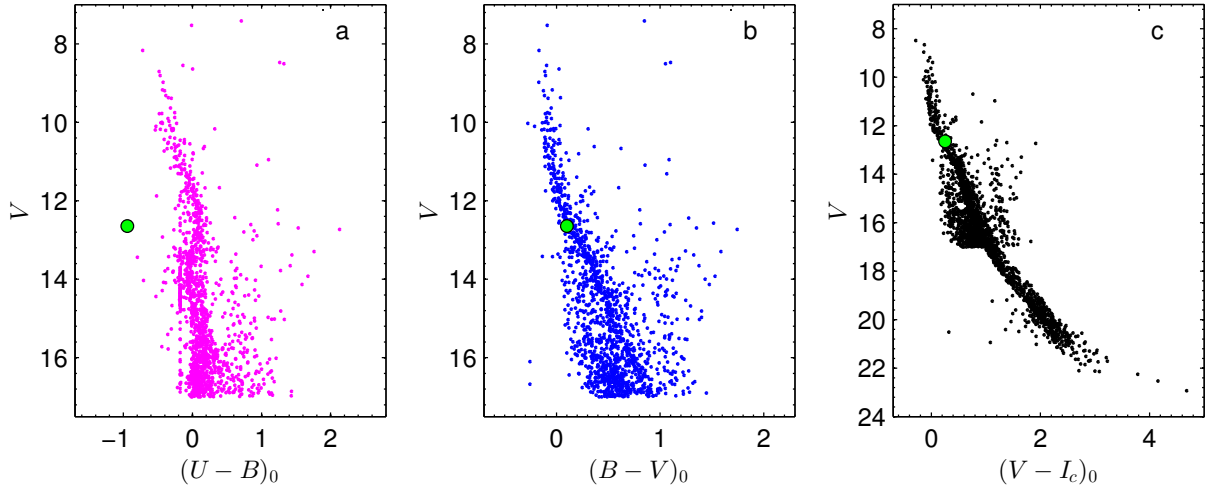


Figure 4.5: This figure displays three different CMDs for the stellar cluster M35; a) $(U - B)_0$ vs. V ; b) $(B - V)_0$ vs. V ; c) $(V - I_c)_0$ vs. V . From a-c the colored marks are samples of 1385, 1306 and 2141 stars of M35, respectively, whereas the green dots represent the star EPIC 209347502. Data for M35 is from the WEBDA database.

$C_1 - C_2$ [25]. For our analysis, photometry in different filters was performed for the target of interest, meaning that $C_1 - C_2$ could be calculated. As can be seen from table 4.2 we have used the two catalog databases *Vizier* at CDS and the Mikulski Archive for Space Telescopes (MAST)⁵ to find the calibrated magnitudes for the two filter systems $UBVR_cI_c$ and $ugriz$ ⁶. Due to the fact that none of the databases have the stellar host's U magnitude we could not immediately find $(U - B)_0$. However, using the following transformation relations we can

$$(B - g)_0 = (0.163 \pm 0.002)(u - g)_0 + (0.170 \pm 0.004), \quad (4.3)$$

$$(U - B)_0 = (0.78 \pm 0.05)(u - g)_0 - (0.88 \pm 0.05). \quad (4.4)$$

Here (4.3) is from [14] and works for Pop-I Main Sequence (MS) stars and (4.4) is from [13] and is valid as long as $R_c - I_c < 1.15$. Thus, we assume that the stellar host is a Pop-I MS star (which we will see later is a good assumption) and we checked the stellar color $R_c - I_c = 0.283$. To take the color reddening into account for the calculation of $(B - g)_0$ in (4.3), $(U - B)_0$ and $(V - I_c)_0$ we used the relation $A_C = R_C E(B - V)$ [19]. From McCall et al.'s paper [19] the extinction coefficient R_C for desired filter C could be found and used. With the knowledge of the calibrated magnitudes for the stellar host from table 4.2 and by using (4.2) we could calculate the following constants $\kappa[(B - g)_0] = 0.295$, $\kappa[(U - B)_0] = 0.692$ and $\kappa[(V - I_c)_0] = 1.356$. As mentioned the uniqueness of discovering a planet orbiting a stellar cluster member is the fact that the distance, d , bolometric correction, BC , color reddening, $E(C_1 - C_2)$, and metallicity, $[Fe/H]$, are often known from previous studies. Accordingly, this is also true for the open cluster M35. Among several studies the most recent parameters found for M35 were used and they can be seen in table 4.3. With all stated information we were able to find $(U - B)_0$, $(B - V)_0$ and $(V - I_c)_0$ both for M35 and the host star.

⁵<http://archive.stsci.edu/>.

⁶Here $UBVR_cI_c$ stands for the following filters, respectively: Ultraviolet, Blue, Visual, Red and Infrared, and the system $ugriz$, which has more defined band limits, was developed for the Sloan Digital Sky Survey (SDSS). For additional filter transformations see <http://sdss3.org/dr8/algorithms/sdssUBVRITransform.php>.

4.4 STELLAR SCIENCE OF HOST STAR

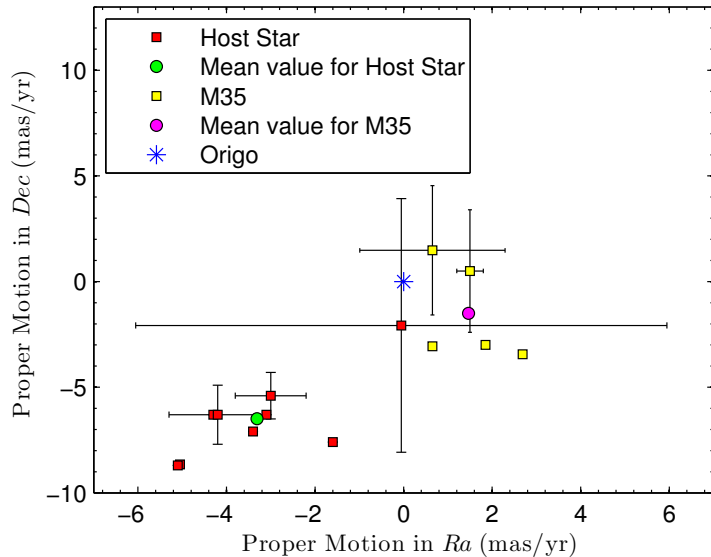


Figure 4.6: This figure shows the proper motion for the host (red squares) and for M35 (yellow squares), where these different measurements are found at Vizier. The mean values of the measurements of the host star (green dot) and M35 (magenta dot) are also represented. For an easier comparison of the amplitude of the proper motions, Origo is shown as well (blue star).

As seen in figure 4.5 we are now able to plot three different CMDs, where the green dots represent the host star and the smaller colored symbols represent presumably stellar members of M35 found at the database WEBDA⁷. From the figure it is evident that mainly the Main Sequence (MS) is visible which is due to the fact that M35 is a relative young stellar cluster. Hence, a substantial number of the stellar cluster members have not evolved to the red giant branch and beyond due to the large timescale (of Gyr) needed. From panel b and c in figure 4.5 it is evident that the stellar host is located on the MS. The largest separation between the host star and the MS can be seen in panel a, where the host star displays an equally large divergence from the MS as a substantial fraction of the represented stars. This divergence may originate from the uncertainties of the conversion calculations, since the derivation of conversion relations between two filter systems in general are complex subjects of study, hence, introducing errors. Even though the $(B - V)_0$ and $(V - I_c)_0$ CMD suggest that the stellar host is a member of M35 the $(U - B)_0$ CMD does not. In total, from figure 4.5 we cannot conclude that the stellar host is a member of M35. However, besides the difficulty to observe in the U -band for ground based telescopes, such a challenge may be worth to realize in order to confirm or disprove the $(U - B)_0$ CMD and, thus, the stellar cluster membership of the host star.

Another profound technique to determine the stellar membership is to see if the proper motion⁸ of the target star is comparable to that of the stellar cluster. Again, a significant difference will indicate that the stellar target is not a member. Figure 4.6 displays recently proper motion measurements both for the target star (red squares) and for M35 (yellow squares). Assuming the mean value of the proper motion measurements for each object is a reliable value for the true proper motion, we have as well plotted these for the host star (green dot) and for M35 (magenta dot). It is evident that the proper motions of the objects are significantly different with a mean value difference between the host star and M35 of about $(\text{pm-Ra}, \text{pm-Dec}) = (4.8, 5.0)$ mas/yr. Thus, this suggests an interstellar field star rather than a stellar cluster member, however, maybe a reliable radial velocity measurement can disprove this statement.

⁷<https://www.univie.ac.at/webda/>.

⁸The observed change in the apparent stellar position in the sky as seen from the Baryoncenter of the solar system, compared to very distant objects.

4.4 STELLAR SCIENCE OF HOST STAR

Having in mind that stellar spectra both can be used to measure the radial velocity as well as to determine the amount of interstellar dust between us and our target of interest, spectra would be valuable to us. By sending a fast-track request to Ditte (a master degree student from Aarhus University) who currently works at the Nordic Optic Telescope (NOT), she was able to make radial velocity measurements of our stellar object of interest. Because this observation was made in the beginning of May, as seen from NOT the object could only be observed for maximum 1 hour just after sunset at a position of 20° - 6° (where the declination angle of 6° is a lower limit for NOT) above the horizon (if desired see figure B.1 for visibility plot and FOV). Consequently, the observation suffers first at all from a very luminous sky background level and secondly from a very high effect of atmospheric disturbance due to the high airmass of the observation. As a result, my supervisors, Frank and Karsten, who analyzed the observed spectra, could unfortunately not with a sufficient precision determine the radial velocity of the stellar host. However, they did observe very strong Natrium lines which normally are indications of a high color reddening [21]. As M35 also has a high color reddening value this indicates that the distance of the two objects is approximately equal. This is due to the fact that the light has to pass equal amount of interstellar gas. Thus, this indicates that the host star is a stellar member of M35. The low quality of the obtained spectra is a motivation to make new spectral observations on this star.

Determination of Stellar Parameters

As mentioned above, two of the CMDs plus the indication of a high color reddening both for the stellar host and the stellar cluster suggest that the host star is a stellar member of M35. However, the $(U - B)_0$ vs. V CMD and proper motion correlation suggest the opposite, hence further validation tests are needed in order to settle this debate. Assuming that the host star is a cluster member, we start by determine fundamental parameters of the stellar host.

The advantage of having a stellar cluster member is that the effective surface temperature can be calculated by the empirical law [25]

$$T_{\text{eff},*} = \frac{5040}{\theta_{\text{eff}}} + P(C, [\text{Fe}/\text{H}]), \quad P = \sum_i P_i C^i. \quad (4.5)$$

Here P is a polynomial function with a power degree depending on the true color, C , and the metallicity, and θ_{eff} is given by

$$\theta_{\text{eff}} = a_0 + a_1 C + a_2 C^2 + a_3 C [\text{Fe}/\text{H}] + a_4 [\text{Fe}/\text{H}] + a_5 [\text{Fe}/\text{H}]^2, \quad (4.6)$$

where $\{a_0, a_1, a_2, a_3, a_4, a_5\}$ are fit-related coefficients, likewise with a dependence of C . The latter equation needs the true color of the star, $C = (B - V)_0$, which we have already estimated in the last subsection. From Ramirez & Malendez's paper [25] two tables (table 2 and 4) representing the coefficients $\{a_0, a_1, a_2, a_3, a_4, a_5\}$ and P_i for dwarf stars were used together with the above represented values for $[\text{Fe}/\text{H}]$ and C . The coefficients P_i were only represented in $[\text{Fe}/\text{H}]$ integer bins, meaning that we choose the coefficients belonging to the closest value of the above given metallicity, which was $[\text{Fe}/\text{H}] = 0.0$. With these coefficients we estimated $T_{\text{eff},*} = (8605 \pm 292)$ K.

The importance of $T_{\text{eff},*}$ is that this parameter can be used to estimate the stellar radius, but some initial steps are needed. First the interstellar extinction must be calculated. With the knowledge of $E(B - V)$ we can estimate the interstellar extinction by

$$A_V = 3.1 E(B - V), \quad (4.7)$$

4.5 EXOPLANET CANDIDATE

Table 4.4: PLANETARY INFORMATIONS FOR EPIC 209347502

Orbital Parameters				Host Star			Exoplanet		
Par	Value	Unit	Par	Value	Unit	Par	Value	Unit	
a	0.0437 ± 0.0093	AU	$T_{\text{eff},*}$	8605 ± 292	K	R_p	1.08 ± 0.23	R_{Jup}	
P	7.5551923 ± 0.0000005	days	L_*	7.52 ± 3.02	L_{\odot}				
i	83.6100 ± 1.8564	deg	R_*	1.23 ± 0.26	R_{\odot}				
e	0		$\bar{\rho}_*$	0.10 ± 0.09	$\bar{\rho}_{\odot}$				

which results in $A_V = (0.7905 \pm 0.0744)$. This substantial value is in agreement with our expectations due to M35 location close to the galactic plane of our Milky Way. As we also know the distance to the object, the absolute visual magnitude can be found by the distance modulus

$$M_V = V - 5 \log(d) + 5 - A_V. \quad (4.8)$$

This yielded $M_V = (2.53 \pm 0.44)$. To find the stellar luminosity and stellar radius the absolute bolometric magnitude, M_{bol} , is needed. Knowing the bolometric correction, BC , we have

$$M_{\text{bol}} = M_V + BC. \quad (4.9)$$

The luminosity is given by

$$L_* = L_{\odot} 10^{\left(\frac{M_{\text{bol},\odot} - M_{\text{bol},*}}{2.5}\right)}, \quad (4.10)$$

where L_{\odot} and $M_{\text{bol},\odot}$ are the luminosity and absolute bolometric magnitude of the Sun, respectively. The result from (4.9) was $M_{\text{bol}} = (2.56 \pm 0.44)$ and from (4.10) was $L_* = (7.52 \pm 3.02) L_{\odot}$. Lastly, using Stefan Boltzmann's law, the radius of the star can be found by

$$R_* = \left(\frac{T_{\text{eff},*}}{T_{\text{eff},\odot}}\right)^{-2} \left(\frac{L_*}{L_{\odot}}\right)^{1/2}, \quad (4.11)$$

where $T_{\text{eff},\odot}$ is the effective surface temperature of the Sun. Our stellar analysis thus yield a stellar radius of $R_* = (1.23 \pm 0.26) R_{\odot}$. The stellar parameters are represented in table 4.4.

Exoplanet Candidate

Model-fit Light Curve

In general taking the effects of Limb Darkening (LD) into account in the transit light curve is not easy and a lot of mathematical modulations are needed in order to do so. The effect on the intensity profile from LD can be described by many laws such as a linear, quadratic, square-root, logarithmic or cubic law. Today, a quadratic intensity profile is often used, however, Southworth [28] found no evident effect in the choice between LD laws.

In the case of the exoplanet candidate a model-fit to the phase folded light curve was performed. Due to the above mentioned mathematical and computational difficulties in model-fitting a transit light curve, we have imported our reduced data to the Exoplanet Transit Database (ETD)⁹, where a model-fit was performed. The ETD model-fit uses a

⁹<http://var2.astro.cz/ETD/>.

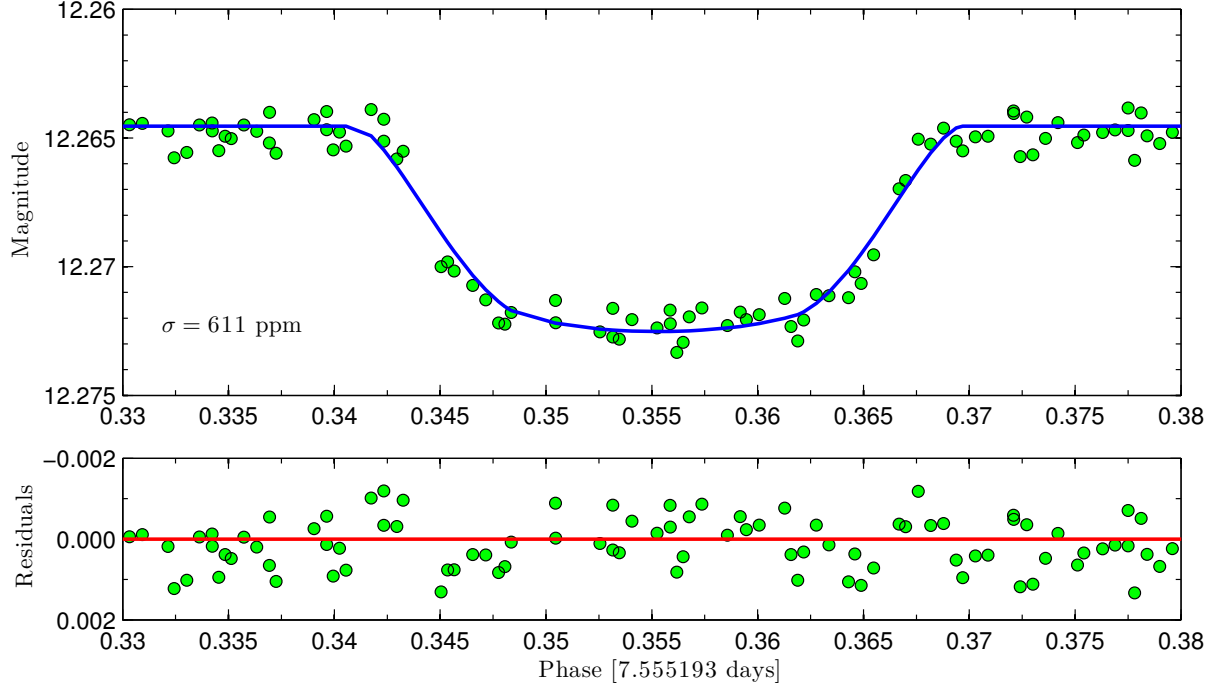


Figure 4.7: This figure displays the phase folded transit light curve of EPIC 209347502. The upper panel displays the transit with the performed model-fit shown as the blue line. The lower panel shows the residuals of the data. The total phase folded light curve shows an uncertainty of $\sigma = 611$ ppm from the model-fit.

simple linear intensity profile, which is given by

$$I(X, Y) = I_0 [1 - \gamma_1(1 - \mu)], \quad (4.12)$$

where I_0 is the mean stellar intensity, γ_1 is a model coefficient and $\mu \equiv \sqrt{1 - X^2 - Y^2}$ is a geometrical function of the transit. In continuation, with the linear intensity profile the ETD server model-fitted our data with the following function

$$m(t_i) = A - 2.5 \log [F(z, k, \gamma_1)] + B(t_i - t_{\text{mean}}) + C(t_i - t_{\text{mean}})^2. \quad (4.13)$$

Here $F(z, k, \gamma_1)$ is a relative flux decrease due to the transit, $z(t_i, t_0, T_{\text{tot}}, b) = D/R_\star$ is the normalized separation of the stellar and planetary centers, D is the center-to-center distance between the star and the planet, $t_i - t_{\text{mean}}$ is the relative time from the mean transit and the coefficients $\{A, B, C\}$ describe zero-point shifts and systematic trends of the magnitude. Linear and quadratic terms in (4.13) are computed with respect to the t_{mean} to suppress numeric errors [23].

The ETD transit simulator assumes that $R_p \ll R_\star$ and the trajectory for the planet over the stellar disk is a straight line [23]. The real struggle of fitting light curves is first of all due to the computation of the normalized separation of the stellar and planetary centers, $z(t_i, t_0, T_{\text{tot}}, b)$, and then the relative flux decrease due to the transit, $F(z, k, \gamma_1)$. Mandel & Agol (2002) [18] were the first to derive these functions in their analytic work on planetary light curves. Later they implemented them computational, and this is what the ETD transit simulator uses. Figure 4.7 shows the model-fit performed by the ETD server to our phase folded light curve. As the transit depth, δ , was estimated from the model-fit we will in the following use this in a *false positive* test.

False Positives

As mentioned in the Introduction, several hundred exoplanets have been confirmed to date, however, astrophysical signals mimicking planetary transits are inevitable among new planet candidates. These mimicking signals are called *false positives* and are results of contaminating variable stars. False positives can be identified through statistical tests and observations. For the validation of the exoplanet candidate, we will here go through some of the used techniques.

Photometric Tests consist most often of seeing-limited observations to identify nearby stars in the photometric aperture. For ground based telescopes seeing-limited images are e.g. achieved by the use of active optics, adaptive optics, speckle imaging and lucky imaging¹⁰. With a seeing-limited image the brightness contribution from nearby stars can be estimated and, thus, be compared to that of the transit depth. A correlation between the two will identify the planet candidate as a false positive.

Binarity Test is an inspection of the presence of an EB system, where both a primary and secondary eclipse are visible. A statistically significant difference between the depth of the transits, will be an indication of a diluted or grazing EB system. However, this technique cannot rule out the possible scenario of a highly eccentric EB system where only one eclipse is visible or the fact that a faint secondary eclipse is lost in the noise.

Spectral Test uses the spectrum of the target star. If the light from a nearby star, weather background or gravitationally bound to the stellar target, falls inside the slit of the used spectrograph, its spectrum will contaminate that of the target star. By looking at wavelength movements of spectral lines, performing a so-called *cross correlation*, this technique may reveal the presence of a double-lined binary system where each line originates from a star.

Photocenter Tests consist of methods to locate the transit source during and near transit events. Two often used techniques are the so-called *flux-weighted centroid* and *different-image* technique. Locating the centroid positions of the transit source less than some σ away from the host star, will in most cases rule out possible mimicking signals from nearby stars [4].

For a photometric test we have inspected images from different surveys at the CDS server and compared these to our own data for stellar contamination (see figure B.2). From the multi-filter red-shift Sloan Digital Sky Survey (SDSS) it is evident that multiple background stars must additively contribute to the combined stellar brightness as they are within the used aperture mask. However, a statistical difference of the transit depths was $< 1\sigma$, where $\sigma = 130$ ppm is the uncertainty of the fitted transit depth. This indicates that there is no evidence of a secondary eclipse which is consistent with the planet interpretation. By checking different databases¹¹ we found no evidence for nearby EB systems within a radius of 30''. Even though a spectral test and a photocenter test may be needed to fully confirm the planet interpretation, our validation test points toward a planet as the transit source, hence, we will continue our study in that belief.

¹⁰For an overview of these techniques see [6].

¹¹Those mentioned in the section of variable findings.

Planetary Parameters

With a model-fit performed to the phase folded transit light curve, as can be seen in figure 4.7, we are now able to determine further planetary parameters. We started by estimating the orbital period of the planet by

$$P = \frac{t(n) - t(0)}{n}, \quad (4.14)$$

where $t(0)$ and $t(n) = t(8)$ are the time of the 1. and 8. transit event, respectively. Both $t(0)$ and $t(n)$ can be measured at conjunction, however, in our analysis they were measured at ingress due to the sharp transition here. Because 8 transiting events were available (as seen in figure 3.5) the orbital period could be determined very precisely to $P = (7.5551923 \pm 0.0000005)$ days. Because we are dealing with a short orbital period exoplanet, it is in our belief that the eccentricity of the orbit is close to zero. This is first of all due to the fact that close-in Keplerian orbits tend to circularize, and secondly because a highly eccentric orbit will bring the likely gas giant close to its host star. This will result in an internal heating of the planet and thus make it difficult to maintain the gaseous envelope [8]. Thus, in the following calculations we will assume $e = 0$.

The best model-fit to the transit from the ETD server gave us the total transit time, $T_{\text{tot}} = (5.18335 \pm 0.07035)$ hours, and the transit depth at mid transit, $\delta = (0.007979 \pm 0.000141)$. However, the model-fit did not provide the full transit time, T_{full} ,¹² which was manually estimated from the figure to be $T_{\text{full}} = (2.5204 \pm 0.0725)$ hours. For consistency we used

$$T_{\text{full}} = \frac{P}{\pi} \sin^{-1} \left(\frac{R_* \sqrt{(1-\eta)^2 - b^2}}{a} \right), \quad (4.15)$$

to calculate T_{full} which yielded a very similar value of $T_{\text{full}} = 2.5370$ hours, hence, justifying the use of our estimate. In (4.15) we used the assumption that $\delta \approx \eta^2$ to estimate $\eta = (0.0893 \pm 0.0008)$. By using the knowledge of R_* and $\eta = R_p/R_*$ the radius of the planet yielded $R_p = (1.08 \pm 0.23) R_{\text{Jup}}$, indicating that the planet is a Jupiter-sized gas giant.

We will now estimate some orbital parameters of the system. By assuming $R_p \ll R_* \ll a$ we found the impact parameter by (2.5)

$$b^2 \approx \frac{(1 - \sqrt{\delta})^2 - (T_{\text{full}}/T_{\text{tot}})^2 (1 + \sqrt{\delta})^2}{1 - (T_{\text{full}}/T_{\text{tot}})^2}, \quad (4.16)$$

which gave $b = (0.848 \pm 0.006)$. Moreover, by rearranging (2.3) and applying $e = 0$ the inclination angle was estimated by

$$i = \cos^{-1} \left(\frac{bR_*}{a} \right), \quad (4.17)$$

yielding $i = (83.6 \pm 1.9)$ deg. From the short orbital period of only about 7.6 days we expect the planet to have a small semimajor axis. We estimated a by rearranging (2.6)

$$a \approx \frac{2\delta^{1/4}}{\pi} \frac{PR_*}{\sqrt{T_{\text{tot}}^2 - T_{\text{full}}^2}}. \quad (4.18)$$

¹²However, the ETD server did provide the time of mid-transit, hence, T_{full} may not be used in the fit.

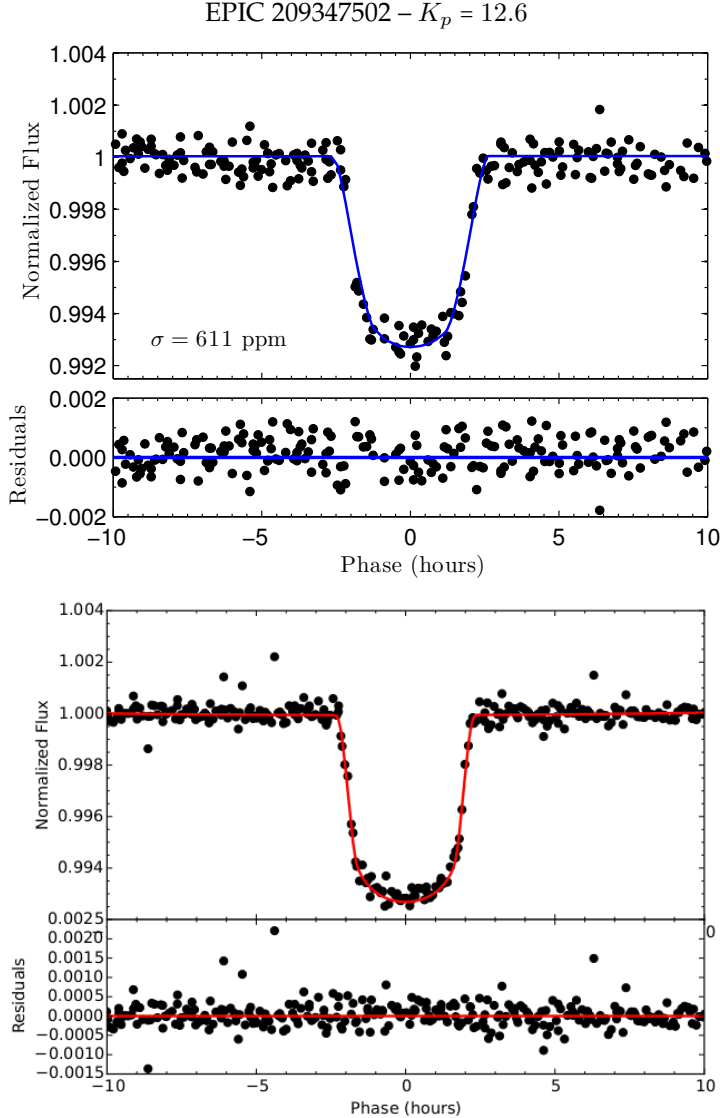


Figure 4.8: These figures display the phase folded light curves of the candidate exoplanet system EPIC 209347502 (or 2MASS 06101557+2436535 from [16]). The upper and lower figure display the transit light curve from this project and from LaCourse et al.'s paper [16], respectively. The blue curve and red curve are model-fits. In each figure the upper panel shows the transiting light curve and the lower panel displays the residuals. To our knowledge, these light curves are the only existing for this specific system.

The result was $a = (0.044 \pm 0.009)$ AU which is in agreement with our expectations. As a last step in our calculations we used (2.9) to estimate the quantity

$$\bar{\rho}_* + \eta^3 \bar{\rho}_p = \frac{3\pi}{GP^2} \left(\frac{a}{R_*} \right)^3, \quad (4.19)$$

which yielded $\bar{\rho}_* + \eta^3 \bar{\rho}_p = (146 \pm 132)$ kg/m³. Since η^3 is usually very small, and in our case of the order 5.1×10^{-5} , the second term on the left side of (4.19) can to a good approximation be neglected. Thus, $\bar{\rho}_*$ can be determined alone from the photometry, which has proven to be very useful for the diagnostic in photometric transit surveys [8]. Applying this approximation the mean stellar density was estimated to yield $\bar{\rho}_* = (0.10 \pm 0.09) \bar{\rho}_\odot$. Because of the large uncertainty of this parameter, additional parameters such as stellar mass were not meaningful to estimate.

As the exoplanet candidate originally was found by LaCourse et al. [16] one month before (Marts, 2015) this project's discovery, we are able to compare, to our knowledge, the only two light curves for this system. For convenience, we have replotted 4.7 together with the transiting light curve from [16] in figure 4.8. For a direct comparison we have adjusted the axis of our light curve so it matches LaCourse et al.'s. The two most obvious differences between the light curve of this project (upper figure) compared to that of LaCourse et al. (lower figure) are first of all their higher photometric precision and secondly the shape of the model-fits. LaCourse's team did not estimate σ of their residuals, however, because the standard deviation of our residuals is $\sigma = 611$ ppm a good estimation for their uncertainty would be about $\sigma \approx 200$ ppm – leaving a factor of 3 in difference.

As seen in figure 4.8 because the photometric precision of LaCourse et al.'s light curve is higher, their model-fit recovers a higher T_{full} than ours. This means that our estimated radius of $R_p = 1.08R_{\text{Jup}}$ or our estimated semimajor axis of $a = 0.04$ AU most likely should be bigger than what LaCourse et al. have obtained. Moreover, our model-fit was made by the assumption that $R_p \ll R_*$ which for a Jupiter-sized planet and a Sun-sized star (e.g. $R_{\text{Jup}}/R_\odot \approx 0.1$) also would give an underestimate of T_{full} .

From a spectral analysis LaCourse and his team determined $T_{\text{eff},*} = 8760$ K indicating that the stellar host is a spectral type A2IV or A2V. However, from their analysis they estimated $R_p = 1.37R_{\text{Jup}}$ and $a = 0.08$ AU which clearly contradicts our expectations. Because our transits are about equally deep their results are logical due to the fact that a bigger semimajor axis is needed to take into account for the larger planet radius, or vice versa. In order to find out what is causing the relative result variations, it should be noticed that by using a higher effective temperature of the host star, just as LaCourse et al. have, and the approach of this project, one will actually find a smaller value of R_p and a than what is estimated in this project - just as we expect. Since we do not know how LaCourse et al. estimated R_p and a , accordingly, our best explanation of the relative variations in results could be the many assumptions we have made – such as $e = 0$ in most of our calculations, $R_p \ll R_* \ll a$ in (4.16) and (4.18), and $\delta = \eta^2$.

For a future project, if a more precise way to determine planetary parameters does exist, this would first of all be desirable. Secondly, in order to determine planetary parameters, a higher photometric precision is needed. Notice that the photometric precision of 611 ppm for our 12.6th magnitude exoplanet system is lower than the median photometric precision of 309 ppm estimated for 12th-13th magnitude stars in Section 4.1. Also, for our planetary study it would might have been in our favor to keep all the course points (resulting from episodes of high instability and thruster firing events) during transiting events. As seen in figure 4.8, this is due to the fact that a more coherent signal of our light curve could be obtained and thus resulting in a better model-fit. However, taking the uncertainty of $0.23R_{\text{Jup}}$ from our estimated planetary radius into account our results are consistent with the interpretation of a hot Jupiter-sized planet.

*"We began as wanderers, and we
are wanderers still. We have
lingered long enough on the shores
of the cosmic ocean. We are ready
at last to set sail for the stars."*

– Carl Sagan, 1980

5

Discussion and Concluding Remarks

The real struggle of analyzing data produced by the Kepler space telescope is due the extremely large pixel size of the spacecraft's CCDs. As experienced in this project, the K2 mission contains additional complications as well as the C0 data and the analyzed FOV within C0. However, because Kepler is not ready to kick the bucket we must find ways to improve, as we will discuss in the following.

Ways to Improve the Photometric Precision

- **Background estimation** was done locally and globally in which the more advanced global subtraction showed to be the better one. However, for TPFs suffering from stellar crowding we noticed an increased noise level in our background estimation – a more detailed understanding of crowding effects must be understood to improve the data quality.
- **Aperture construction** was done with 4 different apertures with sizes depending on K_p . As one would expect, the customized aperture did in most circumstances provide the biggest improvement. This was first of all because a more detailed analysis was gone into its construction and secondly pixels could be removed and added as we pleased, which showed to be important due to the large plate scale. However, in many cases crowding made it difficult to distinguish between target and background polluters, thus, an implementation of the *watershed* algorithm will be needed to separate close targets more precisely.
- **Centroid positions** were measured by the COF. Since a squared aperture which completely covered the target was used, the COF calculation depended heavily on stellar crowding. By letting the number of pixels used in the COF calculation depend on K_p , crowding could to some extend be taken into account. An improvement of the COF routine could first of all be to solely use pixels within a defined mask by the watershed algorithm, which may lower the effect of crowding, and secondly to use a weighted COF estimation. Though, Handberg & Lund found no improvements of the choice of weighting. However, while using the APP algorithm the plot of x_c vs. y_c was not displaying a smooth curve, but a curve with outliers and gaps, accordingly, again due to the large pixels. A possible improvement would might be to use 3D gauss centroids. This was by Vanderburg et al. found to give a better description than the one that the COF gave.

5.2 ASPECTS OF THE FUTURE

- **Include more stars** As only 50 stars were analyzed in this project a higher photometric precision could have been found with a bigger sample. However, this must be a minor effect as a relatively low scatter was found in the σ vs. K_p diagram.
- **The APP routine** did in most cases provide cleaner light curves and a much higher photometric precision compared to what this project's program could extract. However, the majority of the analyzed stars was variable, and as pinpointed by Handberg & Lund the APP provides a higher photometric precision for stellar objects showing minimal variability. Thus, to break down the barrier one would need only to include such "steady" objects. Also, because we efficiently had 3 coherent observations in the C0 data, a possible improvement of the photometric precision could be to use the APP first on each data segment in order to better take different phases of pointing instability into account, for then to use the APP again on the total C0 run for obtaining more coincident flux levels. Notice that the APP will detect sharp features in the light curve like those asteroids make. Hence, asteroid contamination would be a less significant problem in this project.

Aspects of the Future

Given that the study of the analyzed exoplanet candidate heavily relied on the stellar host's membership-likelihood to M35 as well as calculation approximations, these are the ultimate sources of error. At this point, there is a great uncertainty in whether the host star truly is a member of M35 or not, and in order to confirm the membership the following future work are needed: U -band observations of stellar host and radial velocity measurements. Disproving the membership will give rise to a new project: namely to estimate d , $E(B - V)$ and BC in order to estimate planetary parameters. In addition, to fully confirm the planet interpretation of the exoplanet candidate studied in this project, a more extensive false positive analysis is needed. As the quality of the radial velocity measurements applied in this project was not high enough, it will also be a future project to estimate the planetary mass. Lastly, from the results of the photometric precision we showed that there is a trend pointing toward a higher precision for higher magnitude stars compared to expected estimations. This might be an interesting aspect of the K2 mission which is just waiting to be investigated.

Concluding Remarks

As the difficulties in this project were many, we managed to create an efficient routine to extract light curves from the K2 data. We accomplished the goal of this project by proving that the K2 mission harbors conditions for studying a great diversity of astrophysical objects. Our greatest finding was a star of $1.23R_\odot$ hosting a planetary component of $1.08R_{\text{Jup}}$. The exoplanet was found to orbit the stellar host at a distance of 0.04 AU, thus, indicating a hot Jupiter-sized planet. However, a future effort is needed in order to fully confirm the planet interpretation. In this project "*we began as wanderers, and we are wanderers still*".

Bibliography

- [1] D. Armstrong, J. Kirk, K. Lam, J. McCormac, S. Walker, D. Brown, H. Osborn, D. Pollacco, and J. Spake. K2 variable catalogue ii: Variable stars and eclipsing binaries in k2 fields 1 and 0. *arXiv preprint arXiv:1502.04004*, 2015.
- [2] T. Barclay. The kepler guest observer programme. *Proceedings of the International Astronomical Union*, 7(S285):283–285, 2011.
- [3] S. Beucher and C. Lantuéjoul. Use of watersheds in contour detection. In *International workshop on image processing, real-time edge and motion detection*, 1979.
- [4] W. J. Borucki, D. G. Koch, N. Batalha, S. T. Bryson, J. Rowe, F. Fressin, G. Torres, D. A. Caldwell, J. Christensen-Dalsgaard, W. D. Cochran, et al. Kepler-22b: a 2.4 earth-radius planet in the habitable zone of a sun-like star. *The Astrophysical Journal*, 745(2):120, 2012.
- [5] H. Bouy, E. Bertin, D. Barrado, L. Sarro, J. Olivares, E. Moraux, J. Bouvier, J.-C. Cuillandre, A. Ribas, and Y. Beletsky. Messier 35 (ngc2168) dance i. membership, proper motions and multi-wavelength photometry. *arXiv preprint arXiv:1501.04416*, 2015.
- [6] H. Bradt. *Astronomy methods: A physical approach to astronomical observations*. Cambridge University Press, 2004.
- [7] A. Brucalassi, L. Pasquini, R. Saglia, M. Ruiz, P. Bonifacio, L. Bedin, K. Biazzo, C. Melo, C. Lovis, and S. Randich. Three planetary companions around m 67 stars. *Astronomy & Astrophysics*, 561:L9, 2014.
- [8] R. Dotson, S. Seager, et al. *Exoplanets*. University of Arizona Press, 2010.
- [9] P. J. Flower. Transformations from theoretical hertzsprung-russell diagrams to color-magnitude diagrams: effective temperatures, bv colors, and bolometric corrections. *The Astrophysical Journal*, 469:355, 1996.
- [10] D. Foreman-Mackey, B. T. Montet, D. W. Hogg, T. D. Morton, D. Wang, and B. Schölkopf. A systematic search for transiting planets in the k2 data. *arXiv preprint arXiv:1502.04715*, 2015.
- [11] M. C. Fridlund and H. Rauer. The plato mission. In *40th COSPAR Scientific Assembly. Held 2-10 August 2014, in Moscow, Russia, Abstract E1. 14-2-14.*, volume 40, page 896, 2014.

BIBLIOGRAPHY

- [12] R. Handberg and M. Lund. Automated preparation of kepler time series of planet hosts for asteroseismic analysis. *Monthly Notices of the Royal Astronomical Society*, 445(3):2698–2709, 2014.
- [13] S. Jester, D. P. Schneider, G. T. Richards, R. F. Green, M. Schmidt, P. B. Hall, M. A. Strauss, D. E. V. Berk, C. Stoughton, J. E. Gunn, et al. The Sloan digital sky survey view of the palomar-green bright quasar survey. *The Astronomical Journal*, 130(3):873, 2005.
- [14] K. Jordi, E. K. Grebel, and K. Ammon. Empirical color transformations between sdss photometry and other photometric systems. *Astronomy & Astrophysics*, 460(1):339–347, 2006.
- [15] D. Koch, W. Borucki, G. Basri, T. Brown, D. Caldwell, J. Christensen-Dalsgaard, W. Cochran, E. DeVore, E. Dunham, T. N. Gautier, et al. The kepler mission and eclipsing binaries. *Proceedings of the International Astronomical Union*, 2(S240):236–243, 2006.
- [16] D. M. LaCourse, K. J. Jek, T. L. Jacobs, T. Winarski, T. S. Boyajian, S. A. Rappaport, R. Sanchis-Ojeda, K. E. Conroy, L. Nelson, T. Barclay, et al. Kepler eclipsing binary stars. vi. identification of eclipsing binaries in the k2 campaign 0 data-set. *arXiv preprint arXiv:1503.01829*, 2015.
- [17] M. N. Lund, R. Handberg, G. R. Davies, W. J. Chaplin, and C. D. Jones. K2p² – a photometry pipeline for the k2 mission. *arXiv preprint arXiv:1504.05199*, 2015.
- [18] K. Mandel and E. Agol. Analytic light curves for planetary transit searches. *The Astrophysical Journal Letters*, 580(2):L171, 2002.
- [19] M. L. McCall. On determining extinction from reddening. *The Astronomical Journal*, 128(5):2144, 2004.
- [20] B. McNamara, T. Harrison, and B. McArthur. Searching for low-mass binary companions in m35 using the fine guidance sensors of the hubble space telescope. *The Astronomical Journal*, 133(2):394, 2007.
- [21] U. Munari and T. Zwitter. Equivalent width of na i and ki lines and reddening. *Astronomy and Astrophysics*, 318:269–274, 1997.
- [22] D. Nardiello, L. Bedin, V. Nascimbeni, M. Libralato, A. Cunial, G. Piotto, A. Bellini, L. Borsato, K. Brogaard, V. Granata, et al. Variable stars in two open clusters within the kepler 2-campaign-0 field: M 35 and ngc 2158. *arXiv preprint arXiv:1412.5688*, 2014.
- [23] O. Pejcha. Exoplanet transit parameters from amateur astronomers observations, 2008.
- [24] A. Prvsa, K. G. Stassun, S. Bloemen, M. Parvizi, B. Quarles, T. Boyajian, T. Barclay, A. Shporer, D. W. Latham, and M. Abdul-Masih. Kepler eclipsing binary stars. v. identification of 31 eclipsing binaries in the k2 engineering data-set. *arXiv preprint arXiv:1407.3780*, 2014.
- [25] I. Ramírez and J. Meléndez. The effective temperature scale of fgk stars. ii. teff: color:[fe/h] calibrations. *The Astrophysical Journal*, 626(1):465, 2005.

BIBLIOGRAPHY

- [26] G. R. Ricker, D. Latham, R. Vanderspek, K. Ennico, G. Bakos, T. Brown, A. Burgasser, D. Charbonneau, M. Clampin, L. Deming, et al. Transiting exoplanet survey satellite (tess). In *Bulletin of the American Astronomical Society*, volume 42, page 459, 2010.
- [27] D. W. Scott. On optimal and data-based histograms. *Biometrika*, 66(3):605–610, 1979.
- [28] J. Southworth. Homogeneous studies of transiting extrasolar planets—i. light-curve analyses. *Monthly Notices of the Royal Astronomical Society*, 386(3):1644–1666, 2008.
- [29] A. Steinhauer and C. P. Deliyannis. Wiyn/hydra detection of lithium depletion in f stars of the young open cluster m35 and implications for the development of the lithium gap. *The Astrophysical Journal Letters*, 614(1):L65, 2004.
- [30] H. Sung and M. Bessell. Ubvi ccd photometry of m35 (ngc 2168). *Monthly Notices of the Royal Astronomical Society*, 306(2):361–370, 1999.
- [31] R. Szabó, K. Sárneczky, G. M. Szabó, A. Pál, C. P. Kiss, B. Csák, L. Illés, G. Rácz, and L. Kiss. Main-belt asteroids in the k2 engineering field of view. *The Astronomical Journal*, 149(3):112, 2015.
- [32] M. Templeton. Time-series analysis of variable star data. *Journal of the American Association of Variable Star Observers (JAAVSO)*, 32:41–54, 2004.
- [33] A. G. Tielens. *The physics and chemistry of the interstellar medium*. Cambridge University Press, 2005.
- [34] A. Vanderburg and J. A. Johnson. A technique for extracting highly precise photometry for the two-wheeled kepler mission. *arXiv preprint arXiv:1408.3853*, 2014.

A

Appendix: Mission Information

Table A.1: KEPLER INFORMATION

Photometer Aperture	0.95 m
Detectors	95 mega pixels
FOV	126 deg ²
Modules	2 × 21
Plate scale	3.98"
Each modulus	2200 × 1024 pixels
Bandpass	430-890 nm FWHM
Dynamic range	916 mag (V band)

from the international NASA website <http://kepler.nasa.gov/>.

Table A.2: QUALITY FLAGS

Bit	Value	Description
-	0	Good data point.
1	1	Point removed prior to filter as flagged bad data point.
2	2	TPF used to correct jump using constant offset.
3	4	TPF used to correct jump using linear function.
4	8	Data removed as a result of sigma clipping.
5	16	Possible transit structure.

Flags available in the KASOC_FLAGS column in the FITS files. These flags are designated to each TPF and are used for data exclusion. This table is a reproduction of table 2 from [12].

APPENDIX A · APPENDIX: MISSION INFORMATION

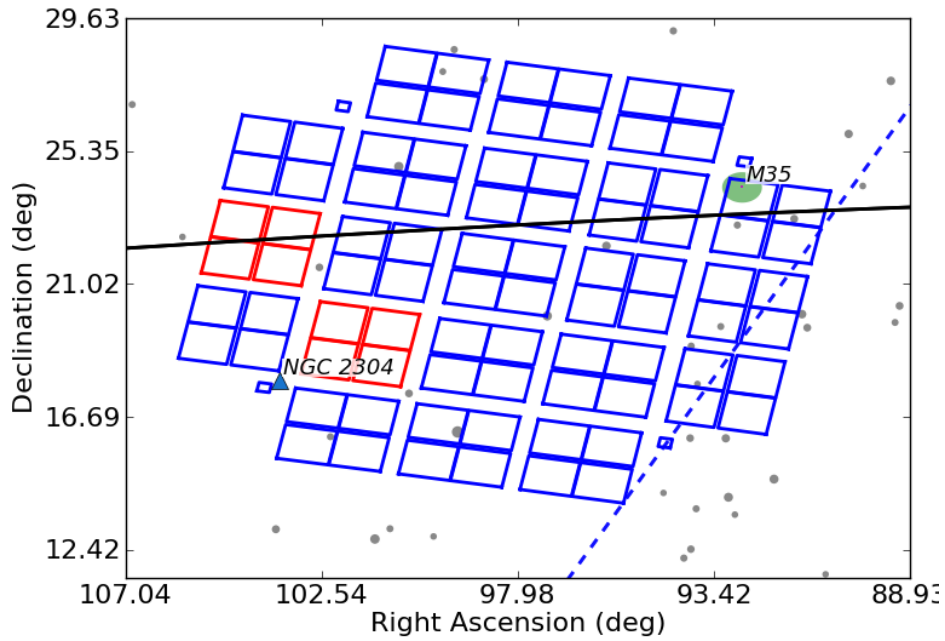
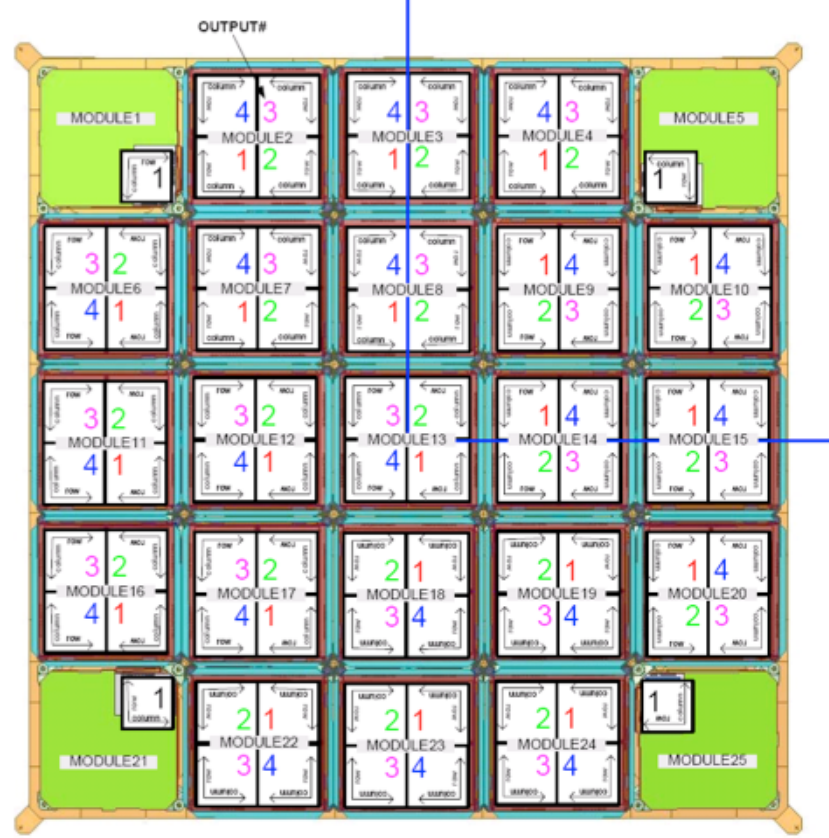


Figure A.1: Information of Kepler and the K2 mission. Top figure display photometric setup of Kepler's CCD's onto 25 modules. Bottom panel shows the full photometric FOV during C0. Here the green dot represents the position of the stellar cluster M35, the red modules indicates nonfunctional modules (module 3 and 7), black line is the ecliptic and the blue dotted line is the galactic plane. The top and bottom figure are from <https://archive.stsci.edu/kepler/> and <http://keplerscience.arc.nasa.gov/>, respectively.

B

Appendix: Project Information

Table B.1: CALIBRATED MAGNITUDE FOR EPIC 209347502

$UBVR_cI_c$ System		$ugriz$ System	
B	13.001 ± 0.014	g	12.769 ± 0.040
V	12.645 ± 0.011		
R_c	12.422 ± 0.010	r	12.495 ± 0.030
I_c	12.139 ± 0.010	i	12.654 ± 0.440

The $UBVR_cI_c$ filter system is from Vizier at CDS and the $ugriz$ filter system is found from the Ecliptic Plane Input Catalog (EPIC) at <http://archive.stsci.edu/k2/epic/>.

Table B.2: PARAMETERS FOR THE OPEN CLUSTER M35

Reference	year	Distance (pc)	Age (Myr)	$E(B - V)$ (mag)	[Fe/H]
Reimers & Koester	1988		70-100		
Sung & Bessell	1999	832 ± 39	200 ± 200	0.255 ± 0.024	
Barrado	2001		180		
Barrado et al.	2001a		>125		-0.21 ± 0.10
Kalirai et al.	2003	912 ± 70	180		
Steinhauer & Deliyannis	2004				-0.143 ± 0.014
Meibom et al.	2009		1.18150716 134-161		
Geller et al.	2010		133		
McNamara et al.	2011	732 ± 145			

This table is a representation of table 1 in [5].

APPENDIX B · APPENDIX: PROJECT INFORMATION

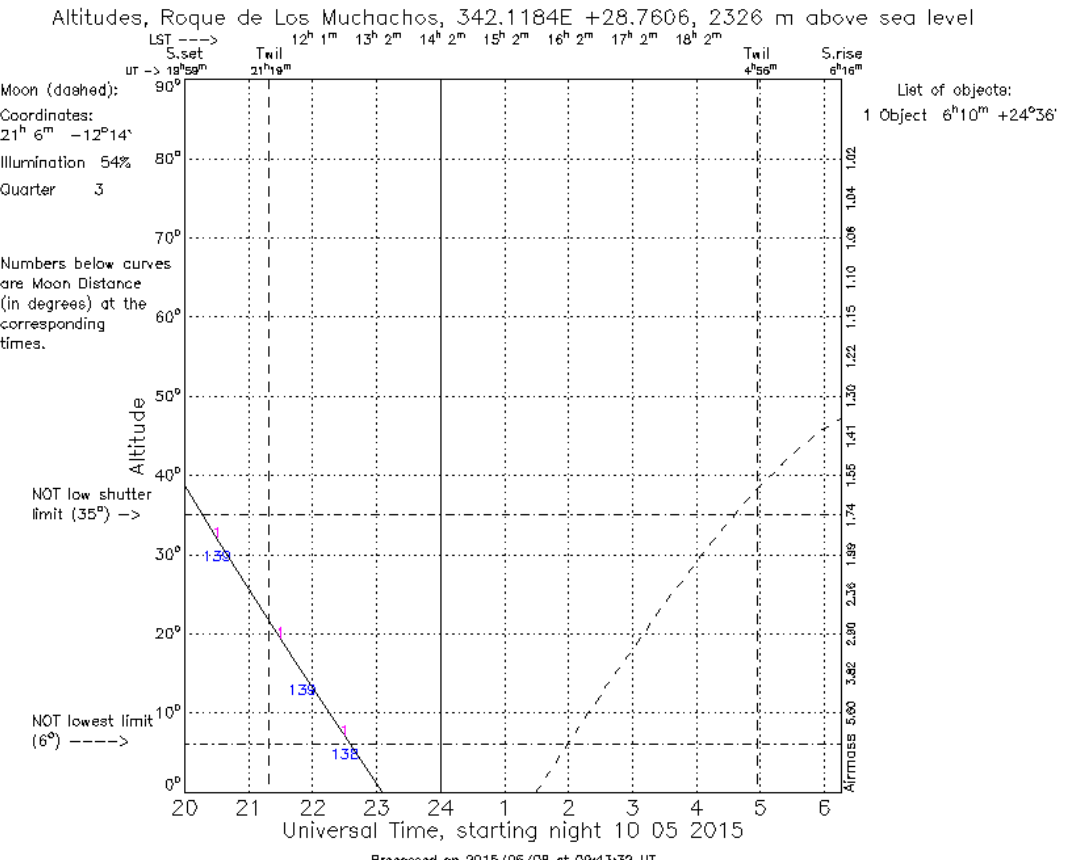


Figure B.1: These figures display the information Ditte used to obtain radial velocity measurements from NOT. The top panel shows the visibility plot from NOT of the night of observation and the bottom panel is an image used to locate and find the target star – a so-called finding chart. The top and bottom figure was provided by this project and the information was found from <http://www.not.iac.es/observing/forms/visibility/> and <http://cds.u-strasbg.fr/>, respectively.

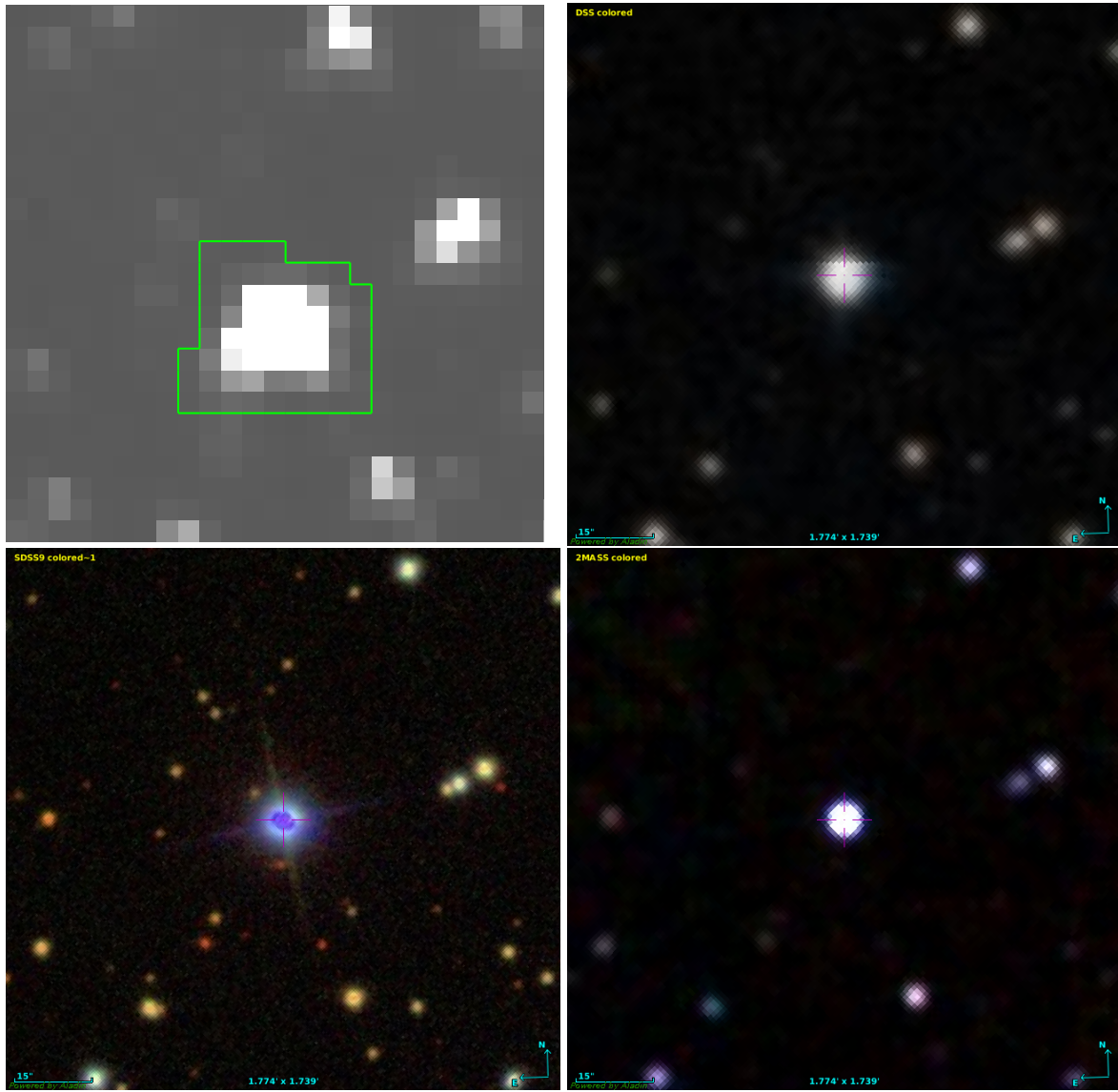


Figure B.2: This figure show 1 summed *K2* image approximately to scale for the 3 images from the CDS server where the central labeled star is the host star EPIC 209347502 of the exoplanet candidate validated in this project. Top left: summed image of target star, where the green line represents our used customized aperture mask; top right: images from the Digital Sky Survey (DSS); bottom left: images from the Sloan Digital Sky Survey (SDSS) which is a multi-filter red-shift survey; bottom right: images from the 2 Micron All-Sky Survey (2MASS) in the *I*-band.

C

Appendix: Results

Table of Findings

Table C.1: TABLE OF KNOWN VARIABLE STARS FROM NARDIELLO ET AL.'S CATALOG

Number in catalog	EPIC	K_p (mag)	α (J2000) (deg)	δ (J2000) (deg)	P (days)	Type
8	209322150	14.527	92.0582	24.5107	2.5100	EB
22	209249175	14.924	92.5170	24.2151	4.4046	Rot
109	209253883	15.010	92.5465	24.2338	3.4522	Rot
161	209301074	17.368	92.4734	24.4246	0.3357	Rot
179	209322888	17.009	92.0671	24.5137	4.6423	Rot
265	209256791	14.689	92.4950	24.2453	5.0078	Rot
267	209257789	14.719	92.5980	24.2493	2.5455	Rot
298	209307833	14.864	92.0492	24.4520	3.7837	Rot
300	209315070	16.210	92.0131	24.4818	7.6177	Rot
330	209307382	14.716	92.4660	24.4502	3.5615	Rot
358	209245653	16.909	92.5218	24.2008	0.5134	Unknown
363	209259635	16.103	92.5596	24.2566	1.2418	Unknown
433	209299651	16.467	92.4667	24.4189	1.8542	Rot
487	209227112	15.642	92.6135	24.1272	4.3270	Rot
513	209269854	13.061	92.4097	24.2982	1.9641	EB

C.1 TABLE OF FINDINGS

Table C.2: TABLE REPRESENTING THE EXOPLANET CANDIDATE

EPIC	K_p (mag)	α (J2000) (deg)	δ (J2000) (deg)	P (days)	Type
209347502	12.563	92.5645	24.6149	7.555193	Exo

Table C.3: TABLE OF NEW VARIABLE STARS

EPIC	K_p (mag)	α (J2000) (deg)	δ (J2000) (deg)	P (days)
209230577	10.941	92.6344	24.1411	—
209250668	12.893	92.5882	24.2210	—
209251714	15.815	92.5159	24.2253	13.1
209257697	14.411	92.6279	24.2490	43.7939
209269368	14.089	92.3732	24.2963	6.2862
209270893	15.361	92.3921	24.3026	4.3674
209310268	12.776	92.5009	24.4619	24.0
209312857	15.037	92.0080	24.4726	18.6085
209315546	14.891	92.0317	24.4835	—
209324795	14.570	92.0831	24.5216	11.0
209326308	13.814	92.5764	24.5279	19.86919
209328999	15.683	92.0672	24.5388	20.7352
209330311	12.107	92.0864	24.5442	21.0
209331823	14.029	92.0710	24.5500	14.9525
209333786	11.582	92.0897	24.5582	6.6
209335463	15.373	92.5753	24.5652	16.45
209344961	15.678	92.3830	24.6041	6.5225
209345412	15.933	92.3500	24.6060	9.7
209345814	15.452	92.3962	24.6076	9.83
—	—	92.0495	24.5457	18.2378

Light Curves

The following lightcurve are all constructed by this project. Every light curve which is showing a already known variable star is discovered by Nardiello et al. [22]. His group have made a web-side where their light curves can be found – see <http://groups.dfa.unipd.it/ESPG/varM35NGC2158.html>.

C.2 LIGHT CURVES

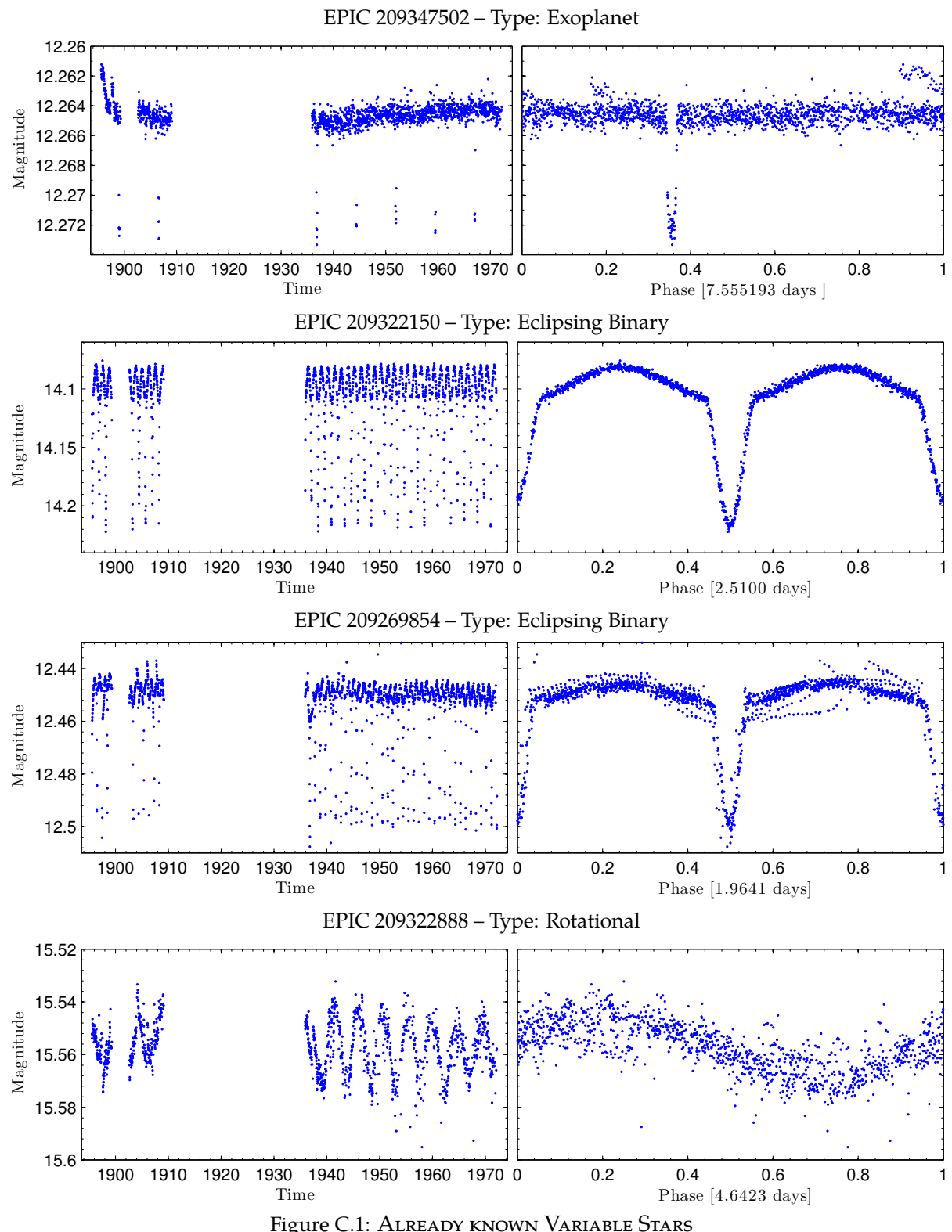


Figure C.1: ALREADY KNOWN VARIABLE STARS

C.2 LIGHT CURVES

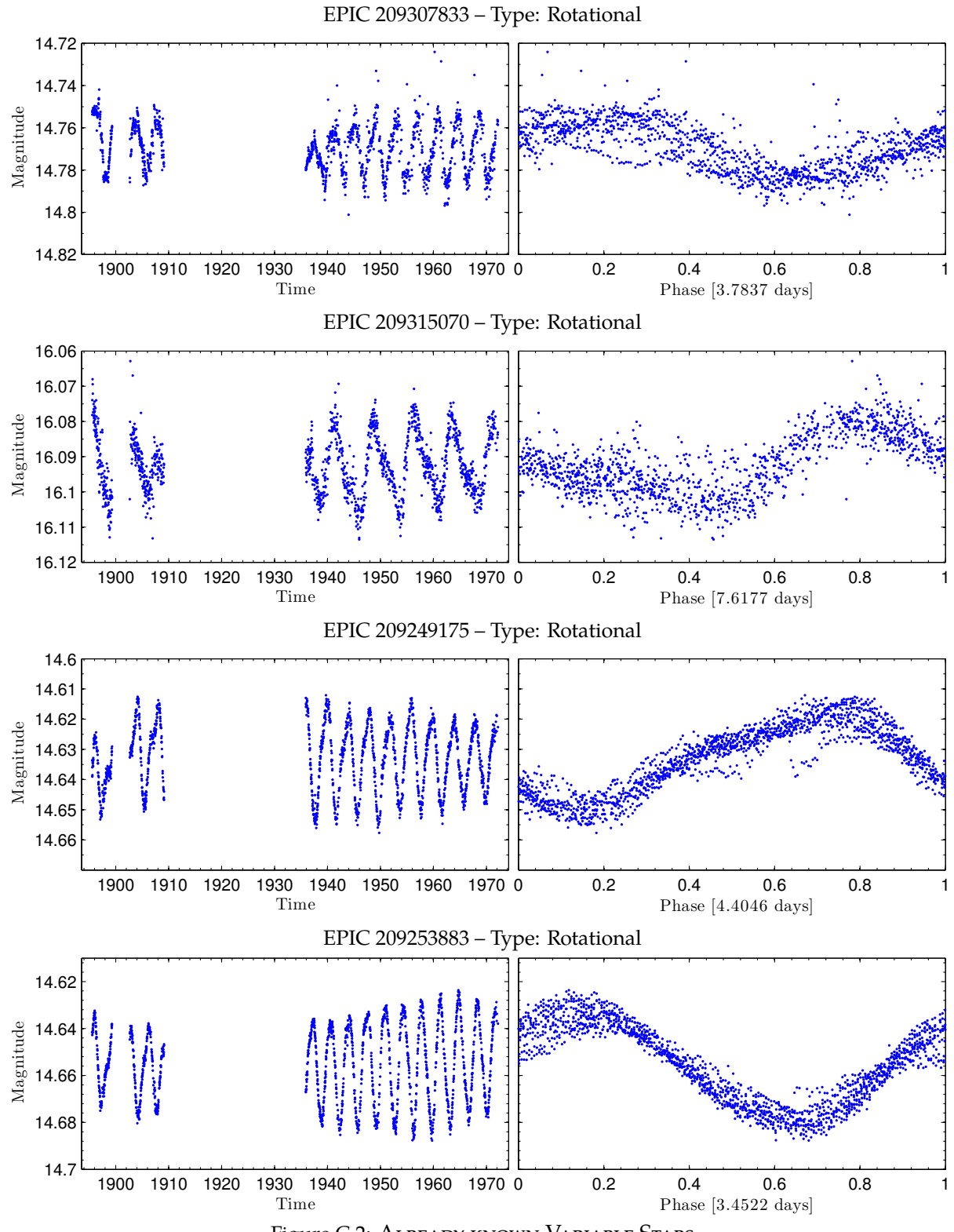


Figure C.2: ALREADY KNOWN VARIABLE STARS

C.2 LIGHT CURVES

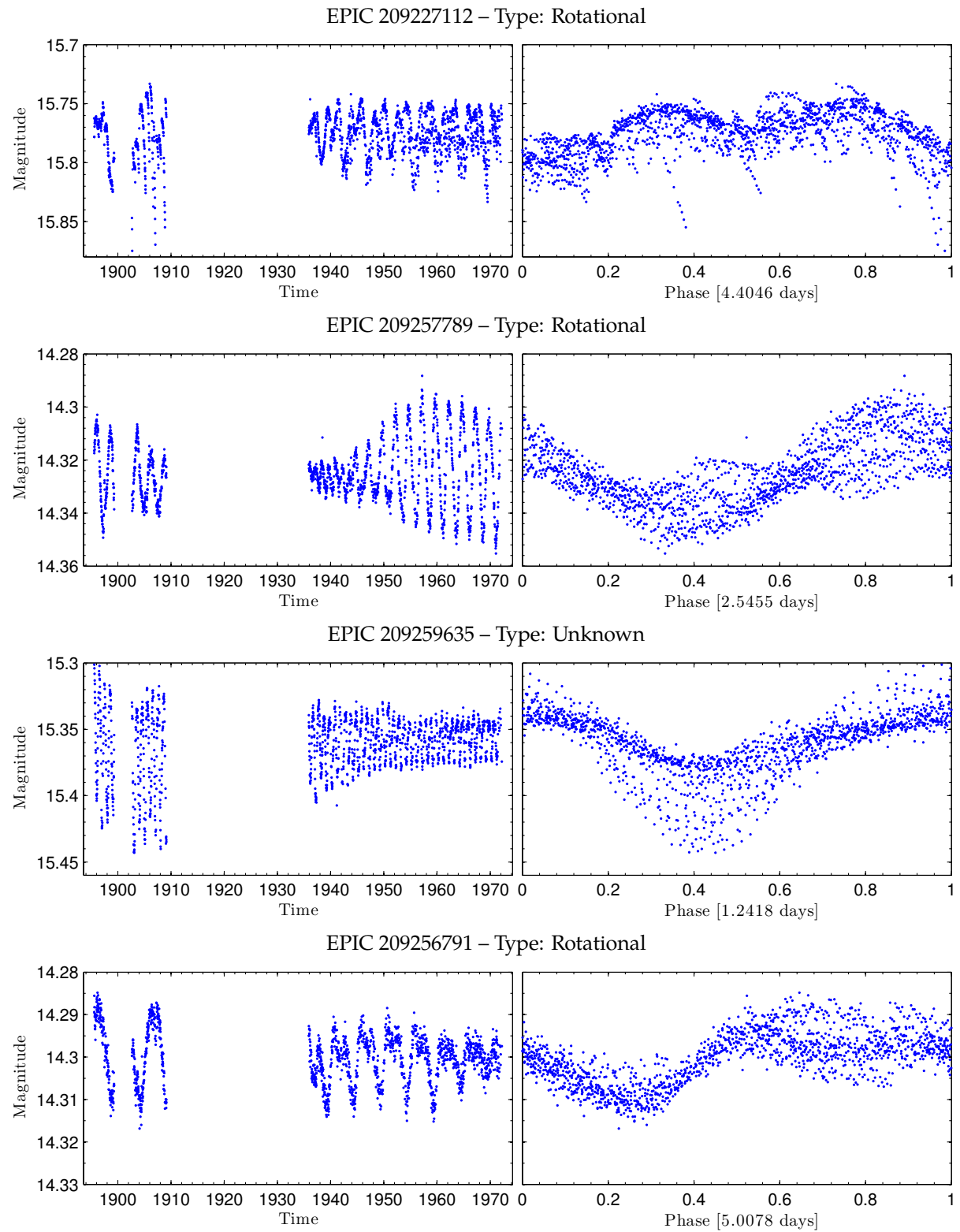


Figure C.3: ALREADY KNOWN VARIABLE STARS

C.2 LIGHT CURVES

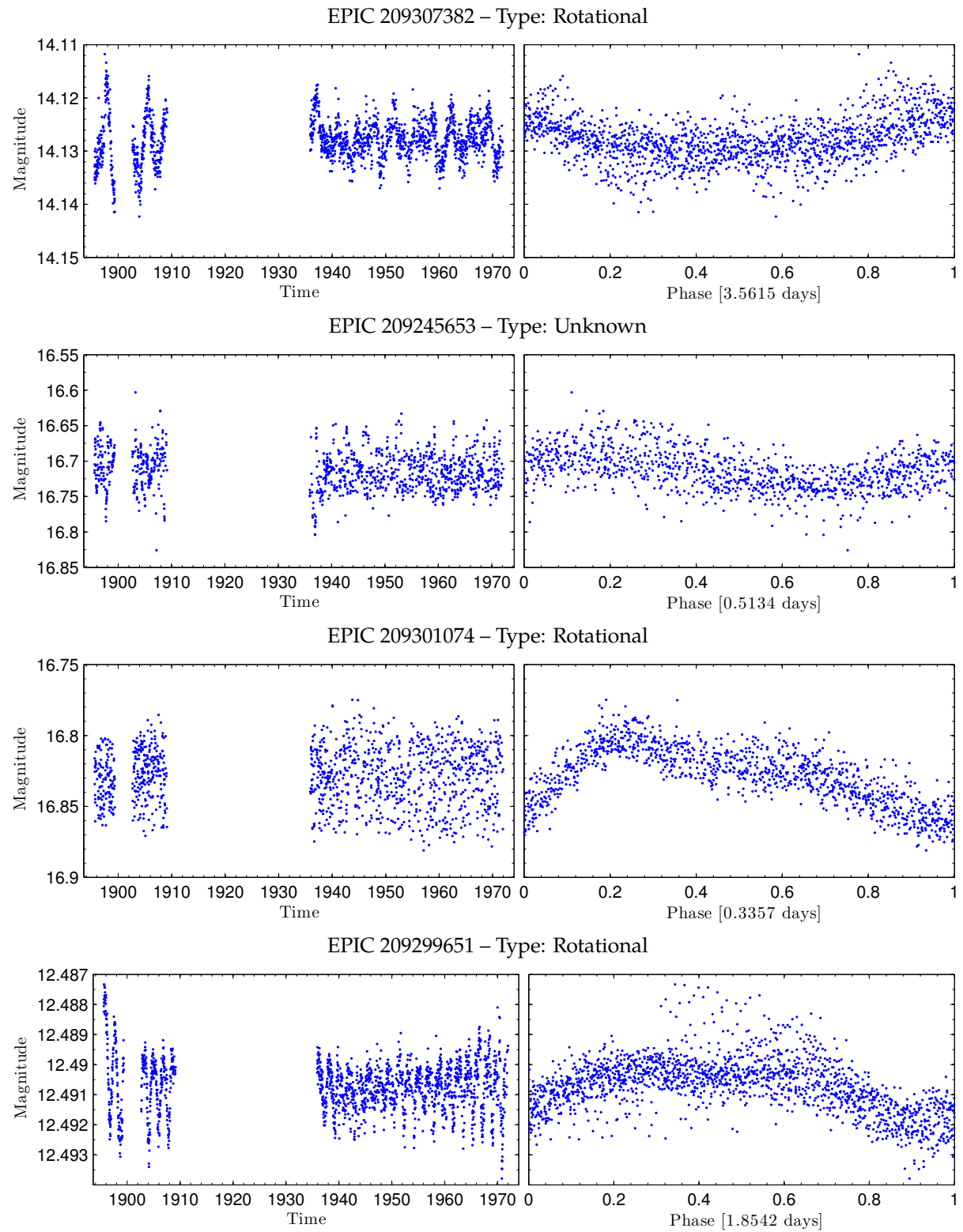


Figure C.4: ALREADY KNOWN VARIABLE STARS

C.2 LIGHT CURVES

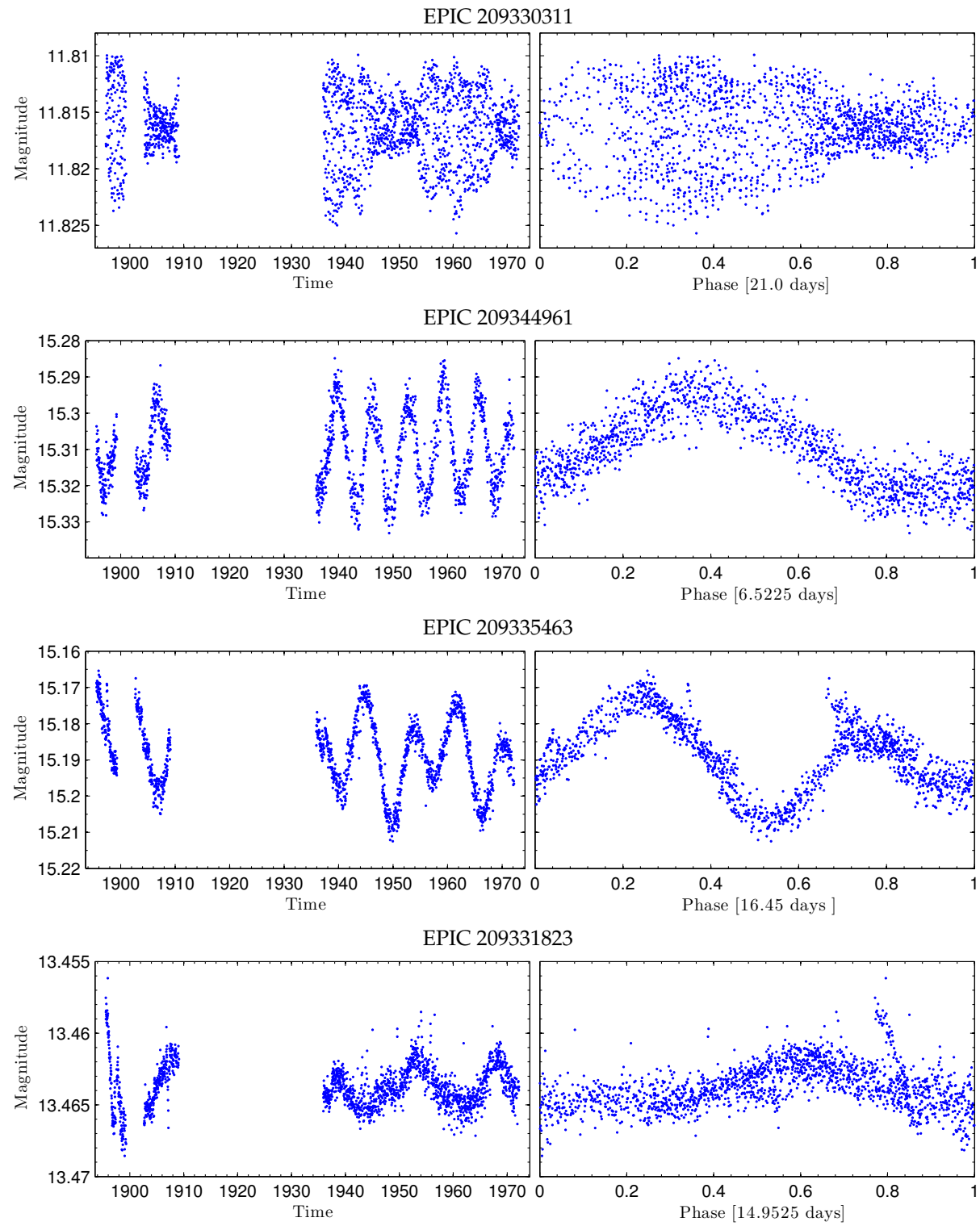


Figure C.5: VARIABLE STARS FOUND IN PROJECT

C.2 LIGHT CURVES

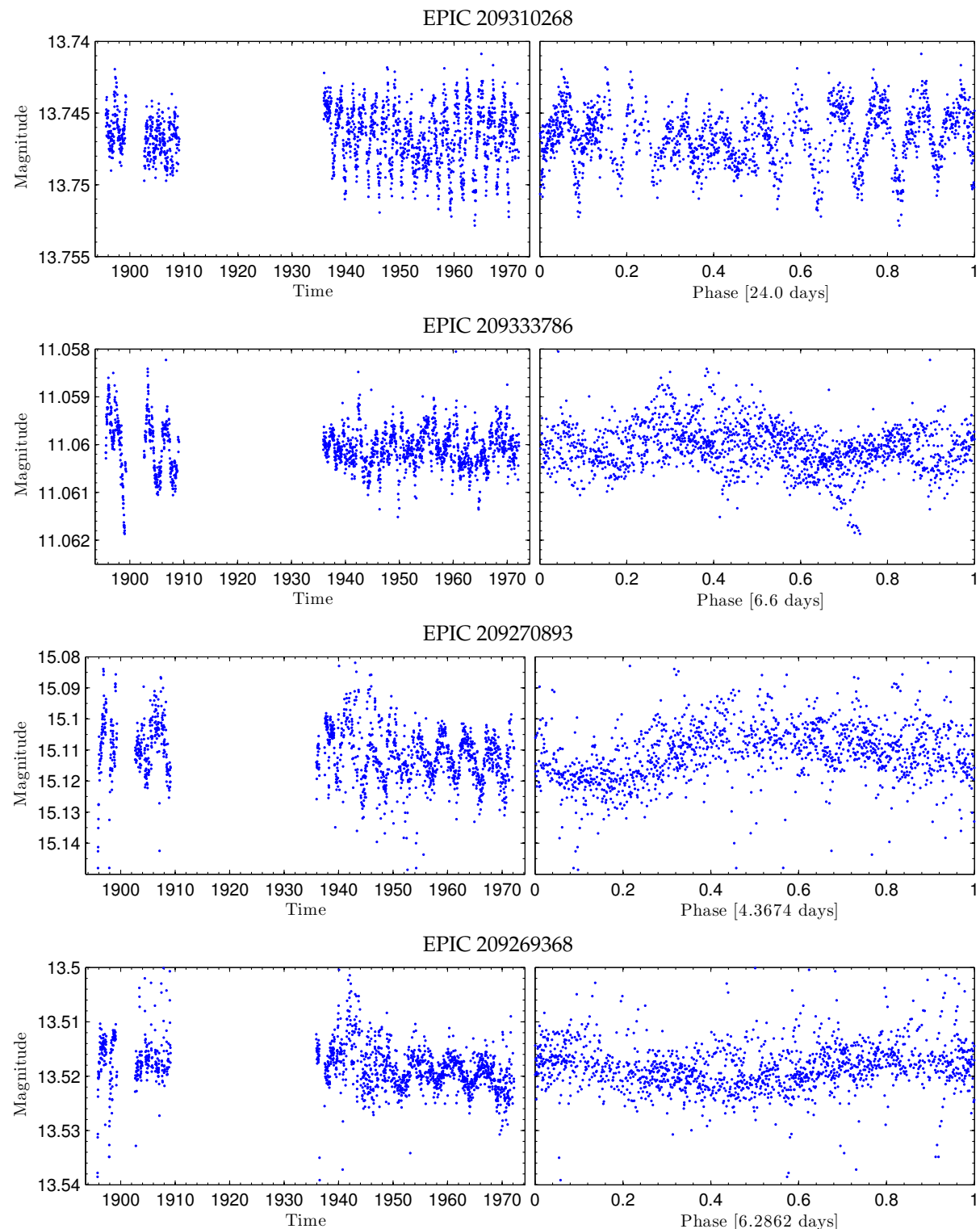


Figure C.6: VARIABLE STARS FOUND IN PROJECT

C.2 LIGHT CURVES

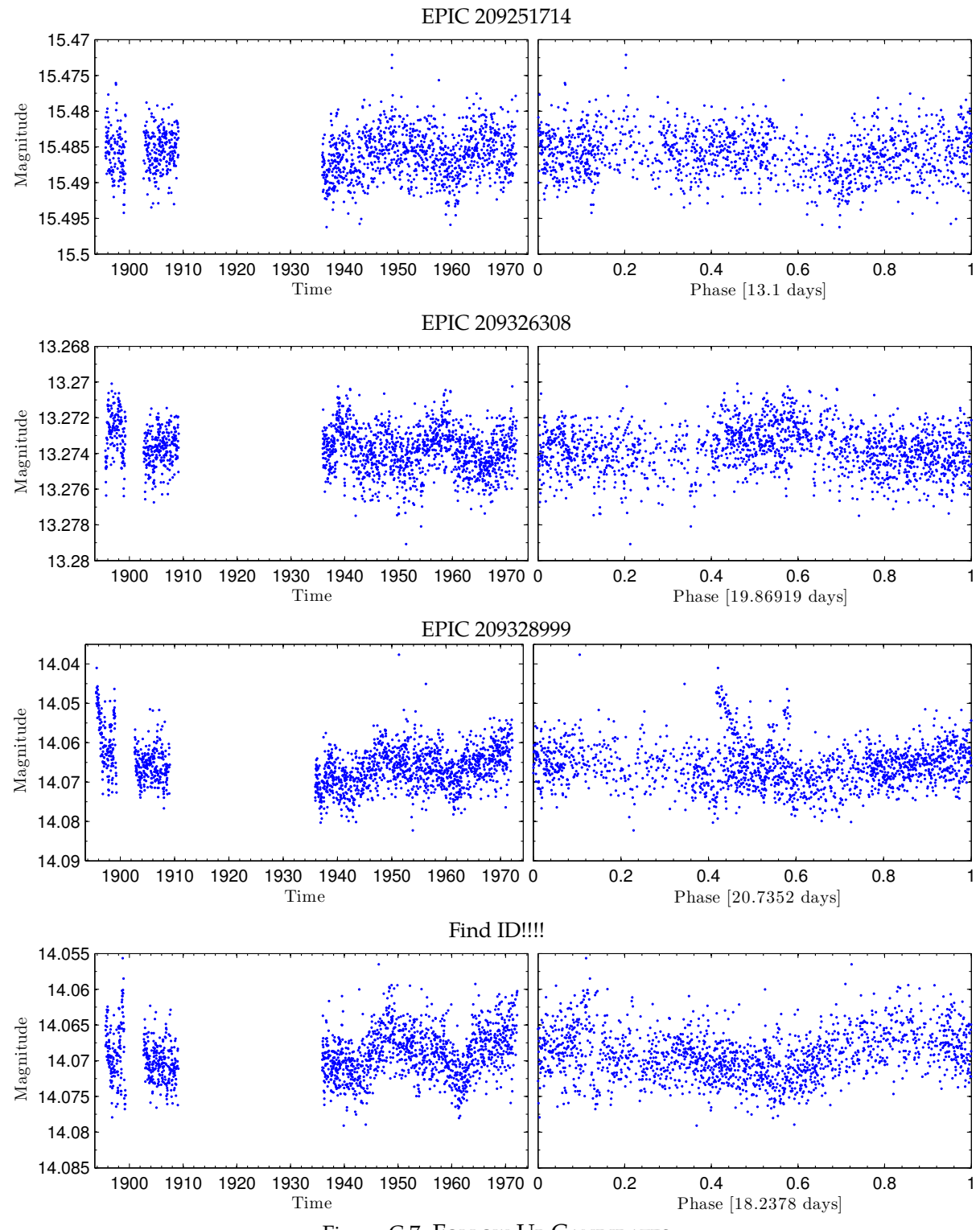


Figure C.7: FOLLOW-UP CANDIDATES

C.2 LIGHT CURVES

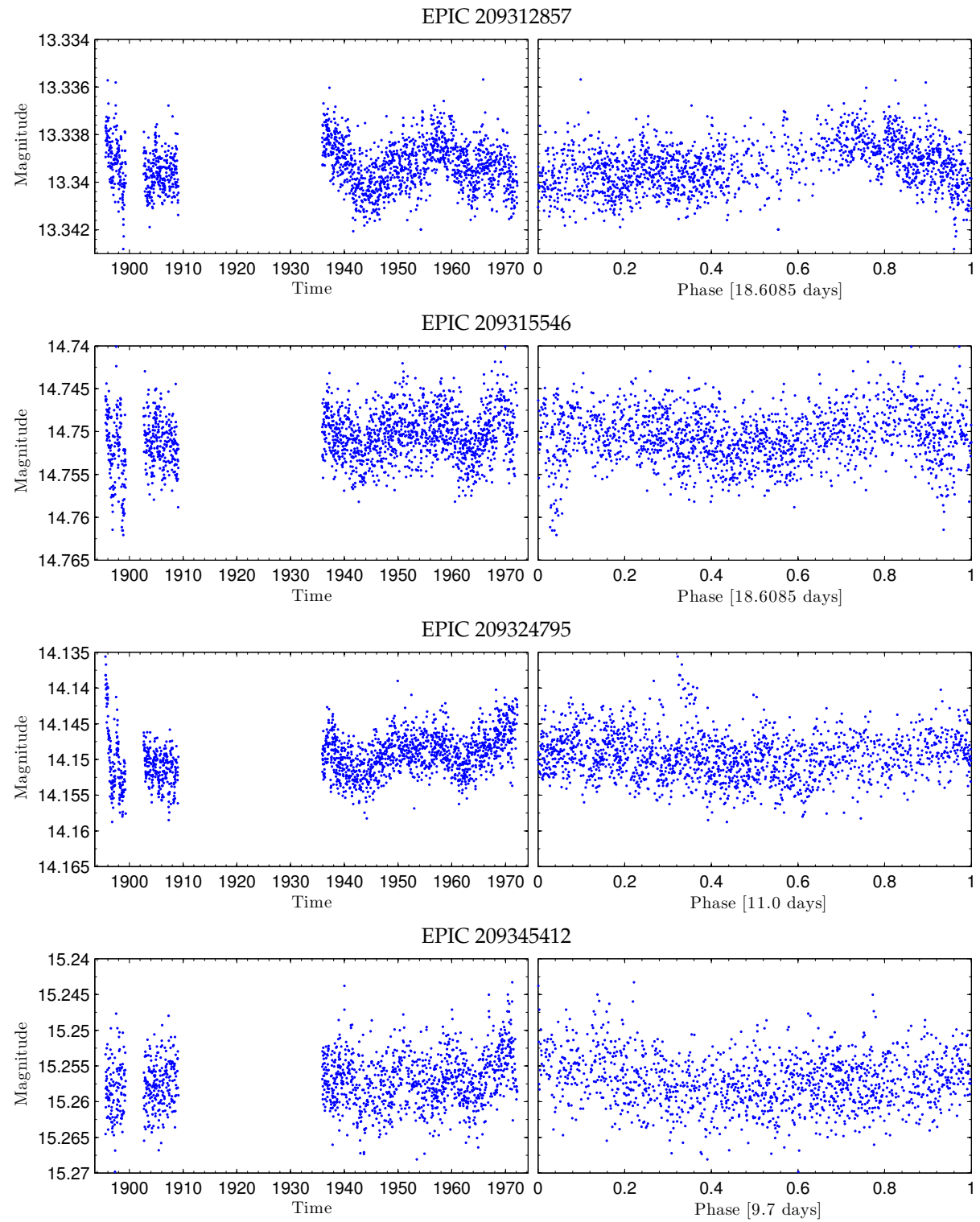


Figure C.8: FOLLOW-UP CANDIDATES

C.2 LIGHT CURVES

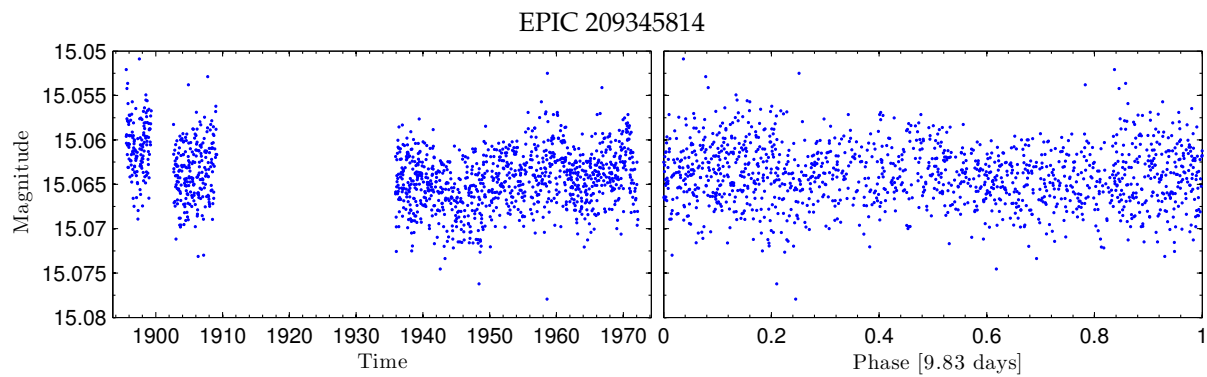


Figure C.9: FOLLOW-UP CANDIDATES

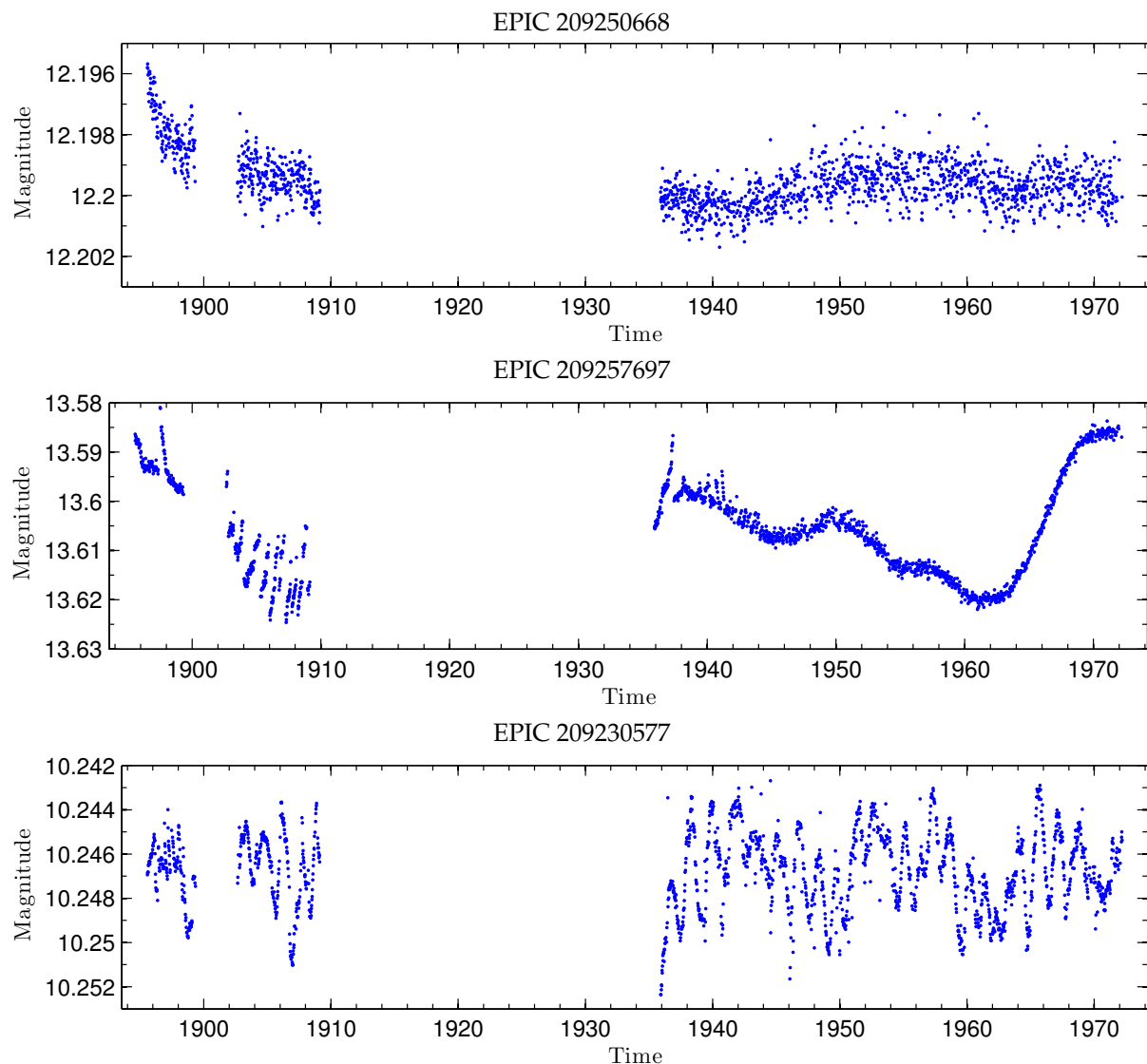


Figure C.10: VARIABLE STARS FOUND IN PROJECT – Unknown periods